

Characterization of the Rotordynamic Forces on Tapered Axial Inducers by Means of a Rotating Dynamometer and High-Speed Movies

Angelo Pasini / Alta S.p.A. *

Lucio Torre / Alta S.p.A.

Angelo Cervone / Alta S.p.A.

Luca d'Agostino / Alta S.p.A. / University of Pisa

* Research Engineer, Via Gherardesca 5, 56121 Ospedaletto, Pisa, Italy; a.pasini@alta-space.com

ABSTRACT

The paper presents the main results of an experimental activity conducted in the Cavitating Pump Rotordynamic Test Facility at ALTA S.p.A. for the characterization of the rotordynamic forces acting on a whirling four-bladed, tapered-hub, variable-pitch inducer, designated as DAPAMITO4. The results obtained by a novel experimental technique, consisting in measuring the continuous spectra of the forces as functions of the whirl ratio, have been compared to high-speed movies taken under forced whirl conditions, in order to get a deeper insight of the role of the structure and oscillating behavior of the cavitating region on the blades. More in detail, a clear relationship between the cavitation structure and the destabilizing peak of the rotordynamic force observed at a positive value of the whirl ratio has been found: the peak appears to be associated to the reorganization of the cavitating regions into a single well defined structure synchronously rotating with the whirl motion; at different values of the whirl ratio, cavitation is broken into several regions which can be associated to backflow vortices.

NOMENCLATURE

A	rotordynamic matrix
A_{ij}	element of the rotordynamic matrix
c	blade chord
c_a	full-blade axial length at tip
D	diffusion factor
F	generalized dimensional force
F^*	generalized nondimensional force
h_m	mean blade height
L	axial length
N	number of blades
p	static pressure
Q	volumetric flow rate
r_H	inducer hub radius
r_T	inducer tip radius
s	azimuthal blade spacing

T	temperature
t	time
α	tip incidence angle
β_b	blade angle w.r.t. the normal to the axial direction
Δp	static pressure rise
Δp_t	total pressure rise
γ	blade angle from axial direction
ε	radius of the whirl orbit (eccentricity)
η	hydraulic efficiency $\eta = Q \Delta p_t / (\tau \Omega)$
Ψ	static head coefficient $\Psi = \Delta p / \rho \Omega^2 r_T^2$
ρ	liquid density
σ	blade solidity = c/s ; cavitation number $\sigma = (p_1 - p_v) / (0.5 \rho \Omega^2 r_T^2)$
τ	torque
Φ	flow coefficient $\Phi = Q / \pi \Omega r_T^3$
ϕ	phase of the rotordynamic force
ω	whirl rotational speed
Ω	inducer rotational speed

Subscripts

D	design conditions
N	normal to the whirl orbit
R	rotordynamic force modulus
T	tip radius/ tangent to the whirl orbit
H	hub radius
x, y	rotating reference frame
X, Y	absolute reference frame
le	blade leading edge
te	blade trailing edge
v	vapor pressure
0	initial condition/ steady forces
1	inlet section

1. INTRODUCTION

Rotordynamic forces are universally recognized as an extremely dangerous source of vibrations in turbomachines and other rotating elements. These forces can affect all the components of the machine, including the bearings, the seals and the impeller itself (Ehrich & Childs [1]).

The rotordynamic forces acting on centrifugal pumps have been widely studied in the past (see for example Hergt & Krieger [2]; Ohashi & Shoji [3]), even if only limited information is available on their dependence on cavitation (Jery [4]; Franz [5]). Recently, Yoshida et al. [6] have investigated the effects of seal geometry on the rotordynamic forces acting on a two-dimensional centrifugal impeller with logarithmic spiral blades, while Suzuki et al. [7] have measured the rotordynamic forces on an artificial heart pump impeller. Experimental data on the influence of cavitation on radial and rotordynamic forces on turbopump impellers mainly come from the work carried out at the California Institute of Technology in the context of the doctoral theses of Jery [4], Franz [5] and Bhattacharyya [8-9]. More recently, at JAXA Kakuda Space Center in Japan, some work has been carried out on whirling axial inducers under cavitating conditions (Yoshida et al. [10]), showing the existence of a strong coupling between a synchronous rotating cavitation observed in the pump and the rotor vibration system. However, presently several aspects related to the rotordynamic forces acting on axial inducers and their correlation with cavitation are not yet perfectly understood.

The rotordynamic configuration of the Cavitating Pump Test Facility (CPTF) at ALTA S.p.A. (Rapposelli et al. [11]) has been designed for the analysis of steady and unsteady fluid forces and moments acting on the impeller as a consequence of its whirl motion under cavitating or fully-wetted flow conditions, with special emphasis on the onset and development of lateral rotordynamic instabilities. Recently, in the framework of a project funded by the European Space Agency, an experimental campaign has been carried out at ALTA S.p.A. on two axial inducers (a three bladed and a four bladed one), aimed at investigating the influence of cavitation on rotordynamic forces by means of forced vibration experiments where the impeller is subject to a whirl motion of given constant eccentricity and angular velocity (Torre et al. [12]; Pasini et al. [13]); some experiments were also carried out by means of a novel testing procedure able to attain the continuous spectrum of the rotordynamic force as a function of the whirl/rotating speed ratio (Torre et al. [14]). In the present paper, the role of the structure and oscillating behavior of the cavitating region on the blades will be analyzed more in detail, by comparing the force measurements on the four-bladed inducer to high-speed movies taken under forced whirl conditions.

2. TEST APPARATUS

ALTA's Cavitating Pump Rotordynamic Test Facility (CPRTF, Figure 1) has been specifically designed for characterizing the performance of cavitating/non-cavitating turbopumps in a wide variety of alternative configurations (axial, radial or mixed flow, with or without an inducer; Rapposelli et al. [11]). The facility operates in water at temperatures up to 90 °C and is readily adaptable to conduct

experimental investigations on virtually any kind of fluid dynamic phenomena relevant to high performance turbopumps. The inlet section is made in transparent Plexiglas and allows for the optical visualization of the cavitation on the test inducer. It can easily be replaced in order to match the tip diameter and clearance of different axial inducers.

The facility is instrumented with a series of transducers for measuring pressures (inducer inlet pressure and static pressure rise; pressure fluctuations in several points close to inducer inlet); flow rates (on the suction and discharge lines); fluid temperatures (inside the main tank and at inducer inlet); absolute angular positions (driving and eccentric shaft).



Figure 1 – The Cavitating Pump Rotordynamic Test Facility.

The test section is equipped with a rotating dynamometer for the measurement of the forces and moments acting on the impeller. A forced whirl motion is obtained by generating the eccentricity by means of a two-shafts mechanism. The two shafts are mounted one inside the other and the whirl motion eccentricity can be finely adjusted before each rotordynamic test in the range between 0 and 2 mm by means of a double eccentric mount. The whirl motion is generated by a brushless motor driving the external shaft, while the impeller rotation is imparted by connecting the internal shaft to the main motor with an omokinetic coupling.

The rotating dynamometer is made of AISI 630 H1025 phase hardening steel and consists of two flanges connected by four posts of square cross-section acting as flexible elements. The posts deformations are measured by 40 semiconductor strain gauges arranged in 10 full Wheatstone bridges, which provide redundant measurements of the forces and moments acting on the impeller. Each bridge is temperature self-compensated up to 120 °C, with separate bipolar excitation and read-out for better reduction of cross-talking. The design of the sensing posts has been carried out as a result of a trade-off between acceptable sensitivity and sufficient structural resistance, operational stability and position control (stiffness). The dynamometer is optimized for a suspended mass of 4 kg with 70 mm gyration radius, an added mass of about 2 kg (based

on the expected magnitude of the rotordynamic forces), a rotational speed of 3000 rpm without eccentricity, and maximum rotational and whirl speeds up to 2000 rpm with 2 mm shaft eccentricity.

Figure 2 shows a rendering of the test chamber assembly used for the experimental campaign. The rotating dynamometer (part 10) is placed between the inducer and the driving shaft. In order to reduce cantilever effects, the inducer has been recessed with respect to the optical access to the test section inlet. In this configuration the inducer blades are contained within the “inlet duct” (part 8). A nominal clearance of 2 mm allows for accommodating sufficiently large whirl eccentricities. The inducer is connected to the dynamometer (part 6) by means of a male/female conical endings adapter (part 4). A fastening shaft (part 1) is coupled on one side by means of a threaded hole machined in the conical interface of the dynamometer and on the other side by means of a nut (part 7).

The relative positions of the inducer (part 3) on the adapter (part 4) and of the adapter on the dynamometer interface (part 6) are guaranteed by means of two pins. A “radial diffuser” (part 5) has been mounted on the test section in order to reduce the suspended mass and minimize the interference with the measurement of the forces acting on the inducer. In order to avoid water sloshing effects in the inducer assembly, e.g. within the nose (part 2), between the inducer and part 1, or between part 1 and part 4, the nose and the conical mounts of the inducer have been sealed by means of o-rings.

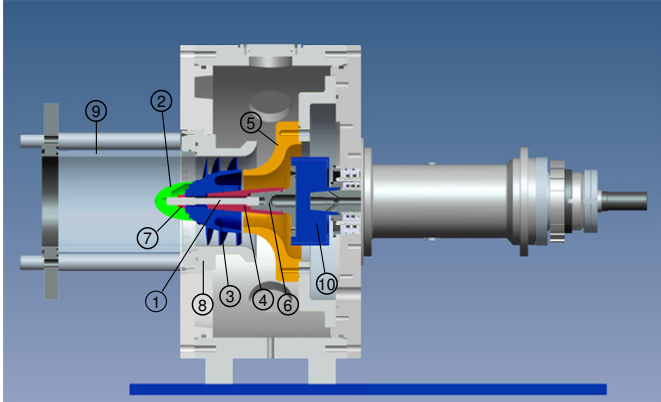


Figure 2 – Rendering of the Test Chamber Assembly.

A Casio Exilim Pro EX-F1 digital photo-camera has been used for taking the high-speed movies shown in the present paper with a resolution up to 336 x 96 pixels at 1200 fps. Despite the low resolution at the highest frame rate, this compact photo-camera allows for taking relatively long movies, and therefore for adequately monitoring the development of the cavitating regions.

3. TEST ITEM

The experimental campaign has been conducted on a four-bladed, tapered-hub, variable-pitch, high-head inducer, named DAPAMITO4 (Figure 3). The test inducer, whose main geometrical and operational parameters are reported in Table 1, has been designed by means of the reduced order model

described in d’Agostino et al. [15-16], and manufactured in 7075-T6 aluminum alloy in order to reduce its weight.

The overall dimensions of this inducer have been chosen for installation and testing in the current CPRTF configuration. A moderate value of the blade loading (with a diffusion factor $D = 0.38$ as defined in d’Agostino et al. [15-16]) and a high solidity ($\sigma_T = 2.25$) have been chosen for reducing the leading-edge cavity and improving the suction performance. The value of the tip incidence-to-blade angle ratio $\alpha/\beta_b < 0.5$ has been selected with the aim of controlling the danger of surge instabilities at design flow under cavitating conditions.

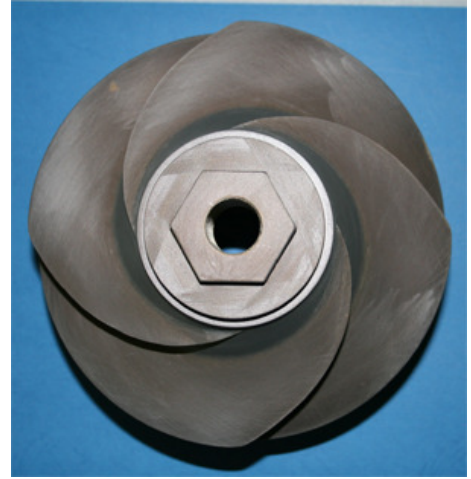


Figure 3 – The DAPAMITO4 inducer.

Design flow coefficient	[--]	Φ_D	0.070
Number of blades	[--]	N	4
Tip radius	mm	r_T	81.0
Inlet tip blade angle	deg	γ_{tle}	81.10
Inlet hub radius (fully-developed blade)	mm	r_{Hle}	48.0
Outlet hub radius	mm	r_{Hte}	58.5
Mean blade height	mm	h_m	27.75
Axial length (fully-developed blade)	mm	c_a	63.5
Inlet hub radius	mm	r_{HI}	35.0
Axial length	mm	L	90.0
Diffusion factor	[--]	D	0.38
Ratio tip incidence / blade angle	[--]	α/β_b	0.31
Tip solidity	[--]	σ_T	2.25
Incidence tip angle @ design	deg	α	2.74
Outlet tip blade angle	deg	γ_{tle}	72.46

Table 1 – Geometrical and operational parameters of the DAPAMITO4 inducer.

For what concerns the inducer performance, Figure 4 shows the noncavitating experimental curves of the DAPAMITO4 in terms of the static head coefficient $\Psi = \Delta p / \rho \Omega^2 r_T^2$ and the hydraulic efficiency $\eta = Q \Delta p_i / (\tau \Omega)$, as functions of the flow

coefficient $\Phi = Q / \pi \Omega r_t^3$. The curves have been obtained for a blade tip clearance equal to 2 mm and for two different values of the water temperature (ambient and about 50 °C). The highest measured efficiency, corresponding to the highest experimental flow coefficient ($\Phi = 0.052$), is about 77%; this value is in good agreement with the typical efficiency observed in this kind of rotating machines ($\approx 70\div 80\%$).

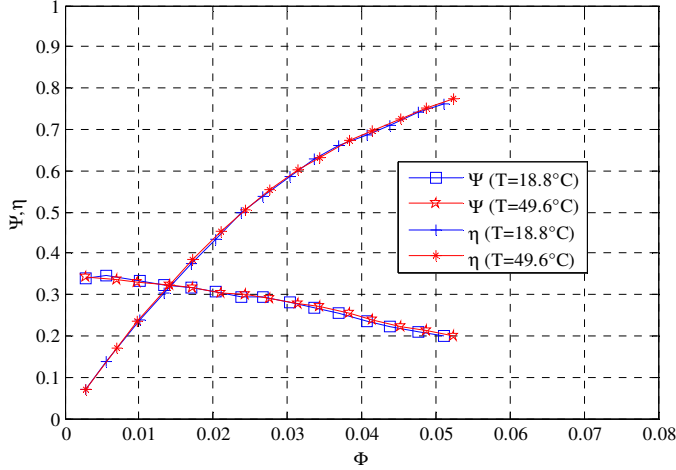


Figure 4 – Noncavitating performance and hydraulic efficiency of the DAPAMITO4 inducer at different water temperatures.

4. EXPERIMENTAL PROCEDURE

The experiments presented in this paper have been conducted under forced vibration conditions, by imposing to the rotor a whirl trajectory represented by a circular orbit of fixed radius.

The generic components of the instantaneous forces acting on a whirling inducer have been schematized in the usual way, as shown in Figure 5. The instantaneous force vector \vec{F} is expressed as the sum of a steady force \vec{F}_0 (not depending on the presence of a whirl motion) and an unsteady force related to the perturbation vector $\vec{\epsilon}$ by means of the rotordynamic matrix \mathbf{A} :

$$\begin{pmatrix} F_x \\ F_y \end{pmatrix} = \begin{pmatrix} F_{0x} \\ F_{0y} \end{pmatrix} + \begin{bmatrix} A_{xx} & A_{xy} \\ A_{yx} & A_{yy} \end{bmatrix} \begin{pmatrix} \epsilon \cos(\omega t + \omega_0) \\ \epsilon \sin(\omega t + \omega_0) \end{pmatrix}$$

where ω_0 is the anomaly of the eccentricity at the initial acquisition time t_0 . Since the rotordynamic matrix \mathbf{A} expresses a rotation + elongation transformation between two coplanar vectors, its elements satisfy the skew-symmetry conditions $A_{xx} = A_{yy}$ and $A_{xy} = -A_{yx}$.

The normal and tangential forces with respect to the circular whirl orbit, F_N and F_T , can be expressed as functions of the elements of the rotordynamic matrix in the following way:

$$F_N = \frac{1}{2} (A_{xx} + A_{yy}) = A_{xx} = A_{yy}$$

$$F_T = \frac{1}{2} (A_{yx} - A_{xy}) = -A_{xy} = A_{yx}$$

In the notation used in the present paper, the normal force F_N is positive when it is in the outward direction, while F_T is positive if it has the same direction as the rotational speed Ω . Therefore a positive tangential force is destabilizing when the directions of the whirl motion and the shaft rotational motion are the same (i.e., the whirl/shaft speed ratio is positive) and stabilizing for a negative value of the whirl/shaft speed ratio. The normal force, conversely, is destabilizing when it is positive and tends to increase the radius of the whirl orbit.

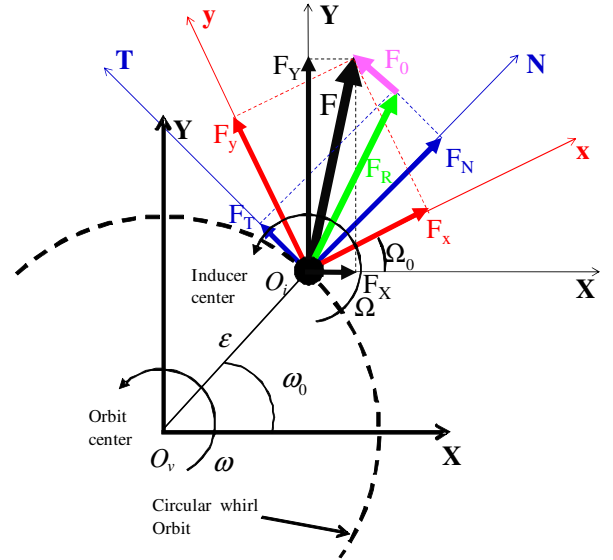


Figure 5 – Rotordynamic forces in the laboratory and rotating reference frames.

The data presented in this paper are referred to purely fluid-induced forces; the effect of buoyancy and tare forces (the inducer dry weight and the centrifugal forces arising by running the inducer in air) have been subtracted from the total force. The unsteady rotordynamic forces have been normalized as follows ([8-9]):

$$F_N^* = \frac{F_N}{\pi \rho c_a \epsilon \Omega^2 r_t^2}$$

$$F_T^* = \frac{F_T}{\pi \rho c_a \epsilon \Omega^2 r_t^2}$$

where ρ is the fluid density, c_a is the axial length of the inducer blades at their tip, ϵ is the radius of the circular whirl orbit (eccentricity), Ω is the inducer rotational speed and r_t is the inducer tip radius.

A novel experimental and data reduction procedure for the characterization of the rotordynamic forces has been recently

developed at ALTA S.p.A., allowing for the measurement of the continuous spectra of the forces as functions of the whirl ratio. This new procedure consists in analyzing the rotordynamic forces in the rotating frame fixed to the dynamometer. In this frame, it can be shown that the forces measured by the dynamometer are linear in the absolute components of the radial force and in the elements of the rotordynamic matrix. This remarkable property can be used to determine the radial force and the rotordynamic matrix by applying a least-square method to the experimental data. All the plots shown in this paper have been obtained by means of this data reduction procedure, which is explained in detail in Torre et al. [14] and will not be illustrated again here.

In the following, the rotordynamic forces are reported both in terms of F_N^* and F_T^* and their non-dimensional modulus $|\vec{F}_R^*| = \sqrt{(F_N^*)^2 + (F_T^*)^2}$ and phase angle ϕ w.r.t. the eccentricity vector \vec{e} , as functions of the whirl ratio ω/Ω . Figure 6 shows, as green, yellow, orange and red areas, the stability regions for positive (top) and negative (bottom) whirl ratios: the same colors have been used in the phase charts for highlighting the behavior of the rotordynamic forces.

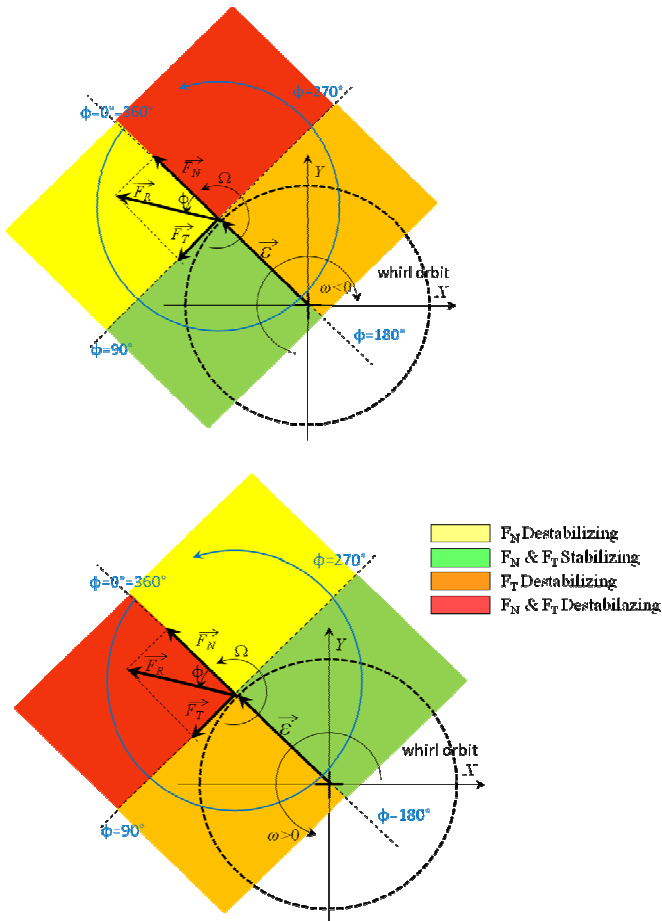


Figure 6 – Schematic representation of the stability regions for the normal and tangential components of the rotordynamic force, for positive (top) and negative (bottom) whirl ratios.

The experiments shown in the present paper have been performed at an inducer rotating speed $\Omega = 1750$ rpm, which represents a compromise value between the generation of measurable rotordynamic forces and the structural integrity of the rotating dynamometer. The eccentricity was equal to $\varepsilon = 1.130$ mm and the flow coefficient was $\Phi = 0.044$. The cavitation number was about $\sigma = 0.09$, corresponding to significantly developed blade cavitation and a head drop equal to 11% of the nominal value (i.e., the inducer was already working under breakdown conditions). In addition, tests have been performed at two different water temperatures: about 20 °C and about 50 °C.

During the tests, high-speed movies of the whirling cavitating inducer have been taken by means of the digital photo-camera, installed in a lateral position with respect to the inlet duct, at a frame rate of 600 fps and a resolution of 432x192 pixels.

5. RESULTS AND DISCUSSION

A thorough experimental campaign for the characterization of the rotordynamic forces on the DAPAMITO4 inducer, conducted at several values of the flow coefficient, the cavitation number and the water temperature, has been presented in detail in Torre et al. [14]. The main results of this test campaign have been as follows:

- The influence of the flow coefficient could be identified in two concomitant effects: as the flow rate decreases the intensity of the rotordynamic force increases, while the spectrum tends to shift towards higher values of the whirl ratio.
- For negative whirl ratios the normal component showed a parabolic behavior, while the tangential one was almost linear; conversely, for positive whirl ratios, both the normal and tangential rotordynamic forces did not show a clear functional dependence on the whirl ratio.
- The intensity of the rotordynamic force clearly showed a minimum and a maximum for positive whirl ratios: the minimum corresponds to an impulsive variation of the angular phase, while the maximum takes place when the rotordynamic force becomes destabilizing.
- Under cavitating conditions, the minimum of the force at positive whirl ratios was found at the same value of ω/Ω , while the maximum was observed at lower values of ω/Ω ; the only stable range for positive whirl ratios was the interval between the minimum and the maximum, while for negative whirl ratios the cavitation tended to reduce the stabilizing range to a small interval close to zero.
- The rotordynamic forces were not affected by water temperature effects up to $T = 50$ °C, under both non-cavitating and cavitating conditions.

In the following Figures, in particular, the results related to the operational point of interest for the present paper ($\Phi = 0.044$, $\sigma = 0.089$, $\varepsilon = 1.130$ mm) are illustrated.

Figures 7 and 8 show the normal and tangential components of the rotordynamic force, while Figures 9 and 10 show its intensity and phase for two different water temperatures. The continuous spectra of the forces are reported together with the discrete results obtained in previous tests by means of the classical data reduction procedure (Pasini et al. [13]): it is worth noticing that the continuous and the discrete results are perfectly superposed, thus confirming the effectiveness of the novel data reduction technique.

As already anticipated, no significant temperature effects can be observed on the force, except for some slight differences in its normal component at negative values of the whirl ratio. The force intensity shows a maximum at $\omega/\Omega = 0.39$ and a minimum, very close to 0, at about $\omega/\Omega = 0.1$ (Figure 9).

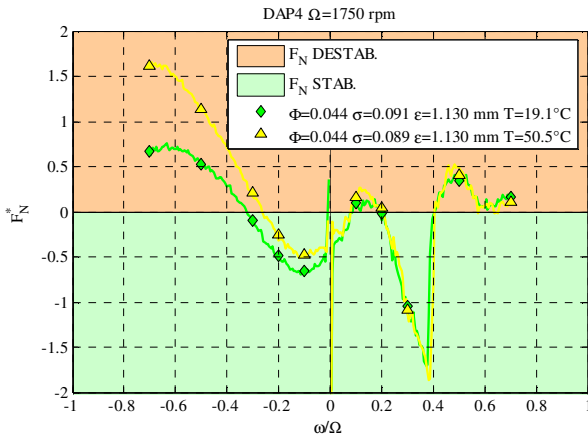


Figure 7 – Normal component of the rotordynamic force, as a function of the whirl ratio, for $\Phi = 0.044$, $\sigma = 0.089$ and two different values of the water temperature.

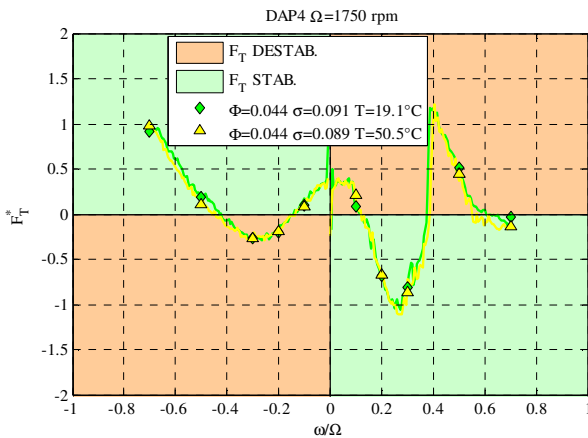


Figure 8 – Tangential component of the rotordynamic force, as a function of the whirl ratio, for $\Phi = 0.044$, $\sigma = 0.089$ and two different values of the water temperature.

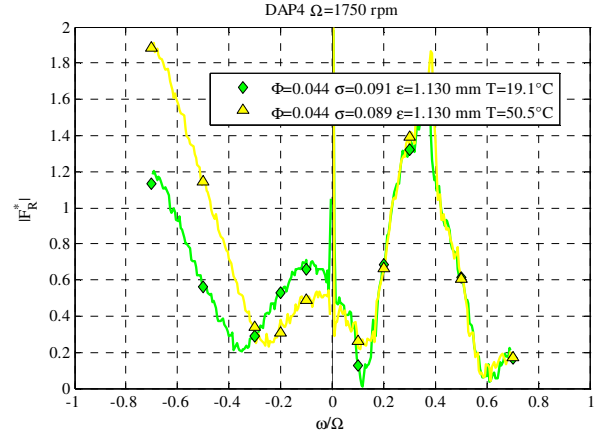


Figure 9 – Intensity of the rotordynamic force, as a function of the whirl ratio, for $\Phi = 0.044$, $\sigma = 0.089$ and two different values of the water temperature.

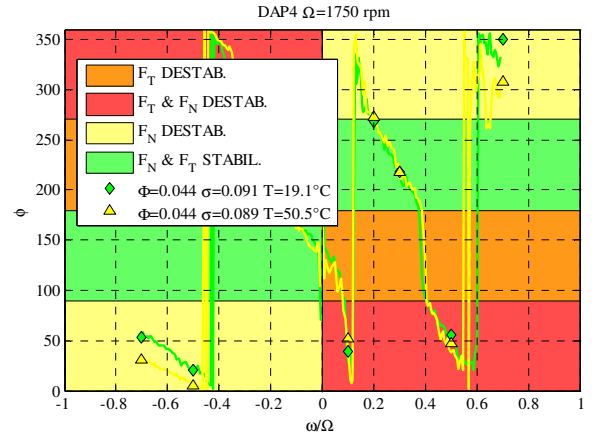


Figure 10 – Phase of the rotordynamic force, as a function of the whirl ratio, for $\Phi = 0.044$, $\sigma = 0.089$ and two different values of the water temperature.

Figure 11 shows the frames extracted from a high-speed movie recorded during the continuous hot test at $\Phi = 0.044$ under cavitating conditions ($\sigma = 0.089$). The frames depict the test inducer at a whirl ratio corresponding to the destabilizing peak of the tangential rotordynamic force shown in Figure 8 ($\omega/\Omega = 0.39$). The cavitating region (highlighted by solid red lines when in the foreground and dotted ones when in the background) appears to be organized in a single structure rotating at the same angular speed of the whirl motion, as shown by the analysis of the extracted frames: since the movie has been recorded at 600 fps and the inducer rotates at $\Omega = 1750$ rpm, a complete whirl orbit at the considered whirl ratio corresponds to 52 frames.

Under different whirling conditions (see Figure 12), the cavitating region does not appear to be solid, but is broken into several structures which change their aspect during the rotation, making it impossible to follow and analyze their paths.

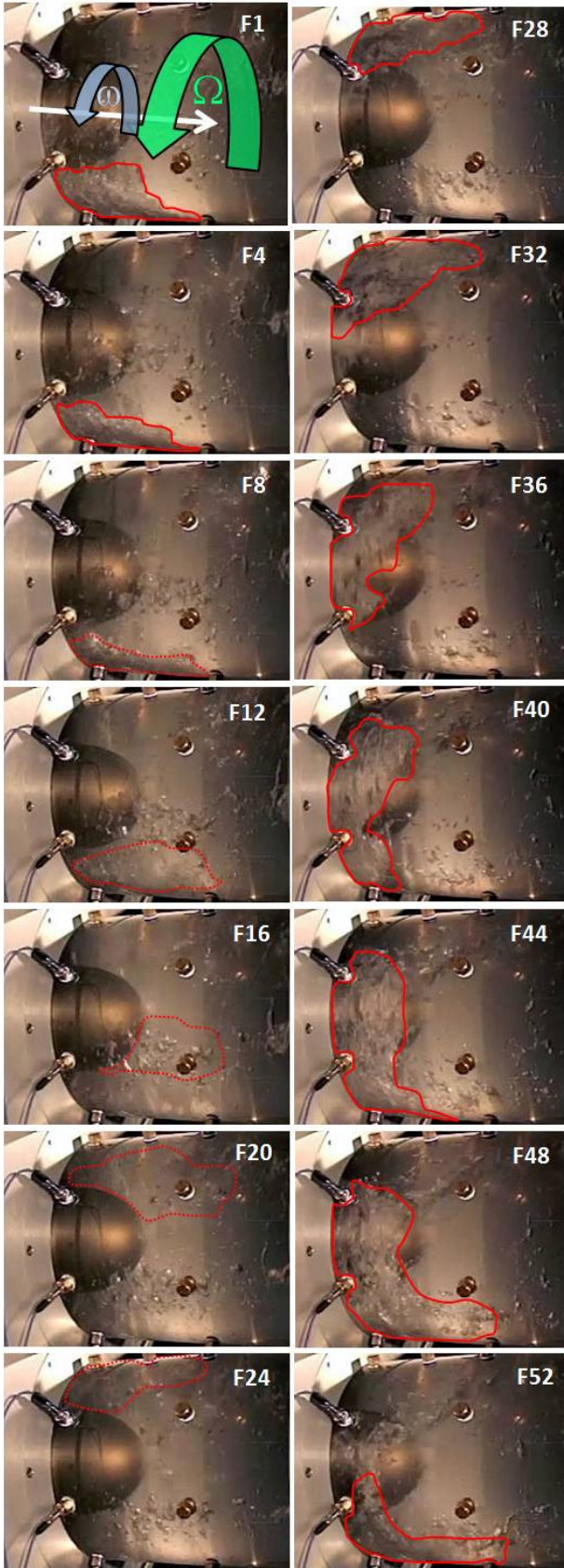


Figure 11 – Frames extracted from a high-speed movie taken at 600 fps ($\omega/\Omega=0.39$, $\Phi=0.044$, $\sigma=0.089$, $T=50.5$ °C).

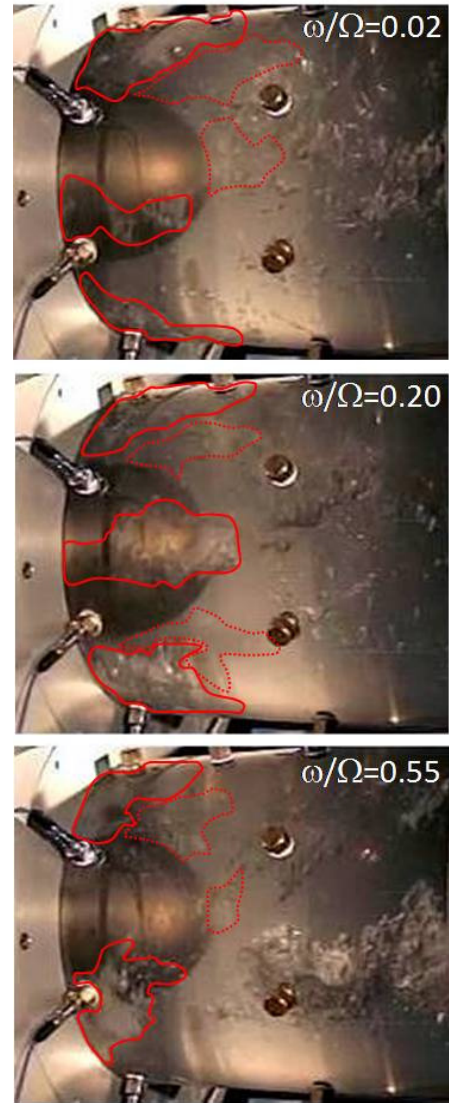


Figure 12 – Appearance of the cavitating regions at different values of the whirl ratio ($\Phi=0.044$, $\sigma=0.089$, $T=50.5$ °C).

Figures 13 and 14 show a combined representation of the information included in Figures 9 and 10. In particular, the rotordynamic force is represented in both intensity and phase for different positive (Figure 13) and negative (Figure 14) whirl ratios. It is worth noticing that the destabilizing force peak has the opposite direction with respect to the whirl eccentricity; furthermore, at the whirl ratio for which the peak is observed, a sudden transition between stabilizing (green) and strongly destabilizing (red) regions occurs.

Conversely, Figures 15 and 16 show the same kind of charts for a noncavitating condition ($\Phi=0.044$, $\sigma=0.918$, $T=50.6$ °C). In this case, the sudden transition from stabilizing to destabilizing conditions is not observed. At negative whirl ratios, the rotordynamic force shows a different behavior between cavitating and non-cavitating conditions: not only the force intensity is higher when cavitation is present, but also its direction is completely different.

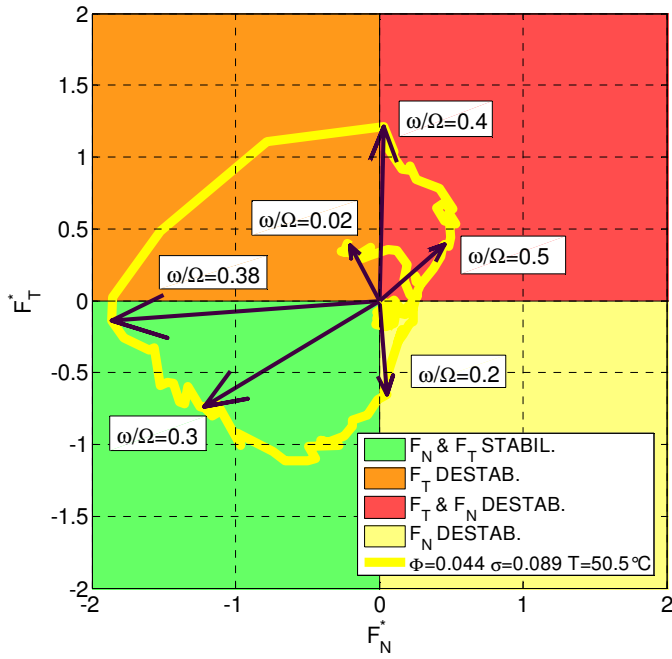


Figure 13 – Rotordynamic force vector in the F_N^* - F_T^* plane for different positive values of the whirl ratio ($\Phi = 0.044$, $\sigma = 0.089$, $T = 50.5$ °C).

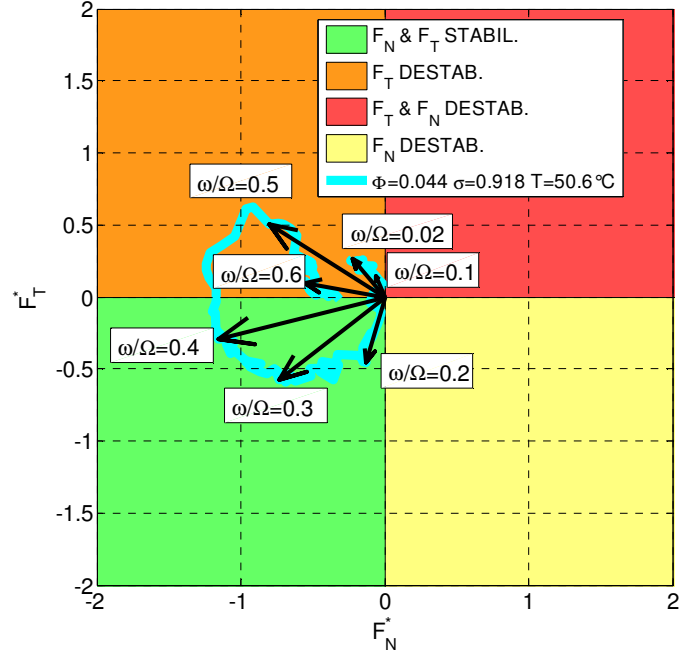


Figure 15 – Rotordynamic force vector in the F_N^* - F_T^* plane for different positive values of the whirl ratio, under noncavitating conditions ($\Phi = 0.044$, $\sigma = 0.918$, $T = 50.6$ °C).

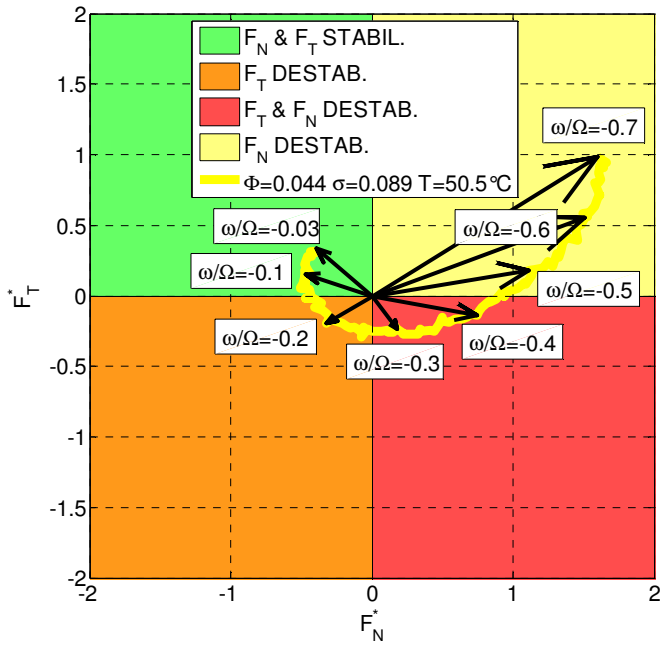


Figure 14 – Rotordynamic force vector in the F_N^* - F_T^* plane for different negative values of the whirl ratio ($\Phi = 0.044$, $\sigma = 0.089$, $T = 50.5$ °C).

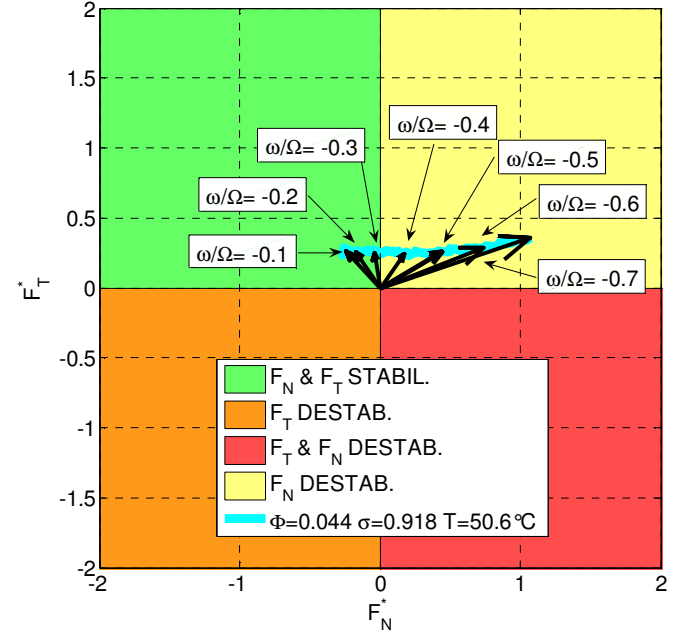


Figure 16 – Rotordynamic force vector in the F_N^* - F_T^* plane for different negative values of the whirl ratio, under noncavitating conditions ($\Phi = 0.044$, $\sigma = 0.918$, $T = 50.6$ °C).

6. CONCLUSIONS

A test campaign for the characterization of the rotordynamic forces on the DAPAMITO4 inducer has been conducted at several values of the flow coefficient, the cavitation number and the water temperature. In particular, the present paper illustrates a comparative analysis of the force measurements taken by means a rotating dynamometer and the optical observation of cavitation from high-speed movies taken by a photo-camera.

Under cavitating conditions, a destabilizing peak of the rotordynamic force has been observed at a positive value of the whirl ratio, and detailed analysis of the high-speed movies has allowed for better understanding this phenomenon. The destabilizing force peak, observed when the force and the whirl eccentricity have opposite directions, seems to be associated to the reorganization of the cavitating regions into a single, well defined structure synchronously rotating with the whirl motion. Conversely, at different values of the whirl ratio, cavitation is broken into several regions which can be associated to backflow vortices. As a confirmation of these findings, a previous experimental characterization of the flow instabilities on the same inducer has shown the onset of a rotating instability connected to the backflow vortices at a frequency comparable to the whirl frequency at which the rotordynamic force peak has been detected.

ACKNOWLEDGMENTS

The present work has been supported by the European Space Agency under Contract No. 20081/06/NL/IA. The authors would like to express their gratitude to Dr. Johan Steelant of ESA-ESTEC, Prof. Mariano Andrenucci and Prof. Fabrizio Paganucci of the Aerospace Department, University of Pisa, Pisa, Italy, for their constant and friendly encouragement. The authors would also like to acknowledge the valuable work of the students who have collaborated to this exciting experimental research: Giovanni Pace, Stefano Bartolini and Luca Pecorari. This paper is dedicated to the memory of our friend and colleague, K. Shinkatsu.

REFERENCES

- [1] Ehrich, F., Childs, S. D., 1984, "Self-Excited Vibrations in High Performance Turbomachinery", *Mechanical Engineering*, May, pp. 66-79.
- [2] Hergt, P., Krieger, P., 1969, "Radial Forces in Centrifugal Pumps with Guide Vanes", *Proc. Inst. Mech. Eng.*, 184, Part 3N, pp. 101-107.
- [3] Ohashi, H., Shoji, H., 1984, "Lateral Fluid Forces Acting on a Whirling Centrifugal Impeller in Vaneless and Vaned Diffuser", *Proc. Workshop on Rotordynamic Instability Problems in High Performance Turbomachinery*, NASA Conf. Publ. 2338, pp. 109-122.
- [4] Jerry, B., 1987, "Experimental Study of Unsteady Hydrodynamic Force Matrices on Whirling Centrifugal Pump Impellers", Report no. 200.22, California Institute of Technology, Pasadena, USA.
- [5] Franz, R. J., 1989, "Experimental Investigation of the Effect of Cavitation on the Rotordynamic Forces on a Whirling Centrifugal Pump Impeller", Ph.D. Thesis, California Institute of Technology, Pasadena, USA.
- [6] Yoshida, Y., Tsujimoto, Y., Morimoto, G., Nishida, H., Morii, S., 2003, "Effects of Seal Geometry on Dynamic Impeller Fluid Forces and Moments", *ASME Journal of Fluids Engineering*, 125, pp. 786-795.
- [7] Suzuki, T., Prunieres, R., Horiguchi, H., Tsukiya, T., Taenaka, Y., Tsujimoto, Y., 2006, "Measurements of Rotordynamic Forces on an Artificial Heart Pump Impeller", *Proc. 23rd IAHR Symposium*, Yokohama, Japan.
- [8] Bhattacharyya, A., 1994, "Internal Flows and Force Matrices in Axial Flow Inducers", Ph. D. Thesis, Report no. E249.18, California Institute of Technology, Pasadena, USA.
- [9] Bhattacharyya, A., Acosta, A. J., Brennen, C. E., Caughey, T. K., 1997, "Rotordynamic Forces in Cavitating Inducers", *ASME Journal of Fluids Engineering*, 119(4), pp.768-774.
- [10] Yoshida, Y., Eguchi, M., Motomura, T., Uchiumi, M., Kure, H., Maruta, Y., 2010, "Rotordynamic Forces Acting on Three-Bladed Inducer under Supersynchronous /Synchronous Rotating Cavitation", *ASME Journal of Fluids Engineering*, 132.
- [11] Rapposelli, E., Cervone, A., d'Agostino, L., 2002, "A New Cavitating Pump Rotordynamic Test Facility", *AIAA Paper 2002-4285*, *Proc.38th AIAA/ASME/SAE/ASEE Joint Propulsion Conference*, Indianapolis, USA.
- [12] Torre, L., Pasini, A., Cervone, A., Pecorari, L., Milani, A., d'Agostino, L., 2010, "Rotordynamic Forces on a Three Bladed Inducer", *Proc. Space Propulsion Conference*, San Sebastian, Spain.
- [13] Pasini, A., Torre, L., Cervone, A., d'Agostino, L., 2010, "Rotordynamic Forces on a Four Bladed Inducer", *Proc. 46th AIAA/ASME/SAE/ASEE Joint Propulsion Conference*, Nashville, USA.
- [14] Torre, L., Pasini, A., Cervone, A., d'Agostino, L., 2011, "Continuous Spectrum of the Rotordynamic Forces on a Four Bladed Inducer", *ASME/JSME/KSME Joint Fluids Engineering Conference*, Hamamatsu, Japan.
- [15] d'Agostino, L., Torre, L., Pasini, A., Cervone, A., 2008, "On the Preliminary Design and Noncavitating Performance of Tapered Axial Inducers", *ASME Journal of Fluids Engineering*, 130(11).
- [16] d'Agostino, L., Torre, L., Pasini, A., Baccarella, D., Cervone, A., Milani, A., 2008, "A Reduced Order Model for Preliminary Design and Performance Prediction of Tapered Inducers: Comparison with Numerical Simulations", *Proc. 44th AIAA/ASME/SAE/ASEE Joint Propulsion Conference*, Hartford, USA.

Numerical Modelling of Cavitation Properties of Mixed-Flow Pump

Milan Sedlář / SIGMA R&D Institute, CZ *

Oldřich Šputa / SIGMA R&D Institute, CZ

Martin Komárek / SIGMA R&D Institute, CZ

* contact email: milan.sedlar@sigma-vvu.cz

ABSTRACT

This paper deals with the CFD analysis of cavitating flow in the mixed-flow pump with the specific speed of 1.64 which suffers from a high level of noise and vibrations close to the optimal flow coefficient ϕ_{BEP} . The peak of the measured noise as well as vibrations is at about 70% of ϕ_{BEP} and both the vibrations and noise are very strong there, especially close to the NPSH value equal to NPSH3.

The ANSYS CFX commercial CFD package has been used to solve URANS equations together with the Rayleigh-Plesset model and the SST-SAS turbulence model has been employed to capture highly unsteady phenomena inside the pump.

The CFD analysis has provided a good picture of the cavitation structures inside the pump and their dynamics for a wide range of flow coefficients and NPSH values, which would be very difficult and expensive to obtain through the experimental research. Cavitation instabilities were detected at the flow rate of $0.7\phi_{BEP}$ close to the NPSH3 value. To verify the numerical analysis, the calculated cavitation performance $\psi(\phi, NPSH)$ has been compared with the available measurements in a closed horizontal plane loop with a good agreement. The calculated results and their frequency analysis also correspond well to the measured noise and vibrations.

NOMENCLATURE

f_Ω	shaft rotational frequency [s^{-1}]
F	force acting on impeller [N]
N	specific speed [-]
NPSH	net positive suction head [m]
NPSH3	net positive suction head required for 3% drop of the pump total head [m]
P	pressure [Pa]
R	radius [m]
Z_I	number of impeller blades [-]
δ	tip clearance [m]
ρ	density of fluid [$kg \cdot m^{-3}$]
ϕ	inlet flow coefficient [-]
ψ	head coefficient [-]
Ω	angular speed [$rad \cdot s^{-1}$]

Subscripts

ax	axial
b	breakdown
exp	experimental

i	inception
out	pump outlet
rad	radial
BEP	best efficiency point
I	impeller
T	tip
1	impeller inlet
2	impeller outlet

1. INTRODUCTION

The mixed-flow pumps often suffer from a very high level of noise and vibrations close to the optimal flow coefficient (ϕ_{BEP}). This negative property can be usually suppressed, but at the cost of decreasing the pump efficiency or a very robust and heavy construction. Of course, both these methods are hardly acceptable for the high performance pumps these days and that is why the detailed knowledge of the noise and vibration sources can be very useful for the pump optimisation.

Recently, many numerical and experimental studies concerning cavitation phenomena in the mixed-flow pumps have appeared, e.g. [1-7], but they are mostly concerned with the steady cavitation. Kobayashi and Chiba [8] modelled unsteady hydraulic forces acting on the impeller of a mixed-flow pump operated under cavitation using the Large Eddy Simulations (LES) while Yamamoto and Tsujimoto [9] studied experimentally the cavitation surge in a centrifugal pump. Nevertheless there is still lack of information in the literature concerning cavitation instabilities in the mixed-flow or radial-flow pumps. Practically all studies dealing with these instabilities are devoted to inducers, which represent a special type of the axial-flow pumps. When operating under cavitation, inducers can suffer from a wide range of cavitation instabilities (Kamijo et al. [10] or Tsujimoto et al. [11]), even at the design flow rate. These instabilities generate oscillations dangerous for the machine operation, especially at high rotational speeds. One of the diagnostics which is used to determinate the type of cavitation instability is the frequency analysis. We have to examine dominant frequencies and compare them with the rotational frequency f_Ω as well as the fundamental frequency of inducer blade passage excitation. The following table comes from the works of Brennen [12] and Tsujimoto et al. [11], [13-14] and shows typical frequencies of some cavitation instabilities in the inducers:

Instability	Frequency Range
rotating cavitation	$1.1f_{\Omega} - 1.3f_{\Omega}$
rotation cavitation, backward travelling mode	$0.9f_{\Omega}$
partial cavitation oscillation	$< f_{\Omega}$
cavitation in backflow vortices	$0.16n f_{\Omega} - 0.21n f_{\Omega}$, n being number of vortices
attached uneven cavitation	f_{Ω}

To examine the unsteady cavitating performance, experimental methods have been widely used for a long time. Recently the progress in development of CFD tools has encouraged authors to examine unsteady cavitation phenomena in the numerical way (e.g. Berntsen et al. [15], Bouziad [16] or Tsujimoto et al. [17-18]). These numerical tests indicate that there are limitations in modelling of cavitation instabilities using URANS (Unsteady Reynolds-Averaged Navier-Stokes) based codes and that the future work will tend to the Large Eddy Simulations (LES), though they are still far from current engineering practice.

2. DESCRIPTION OF PUMP AND NUMERICAL PROCEDURE

The pump which is an object of this paper has the dimensionless specific speed $N = 1.64$ and is produced in two configurations: with a volute (Fig. 1) or the axial diffuser (with nine vanes) and 90° elbow (Fig. 2). The mixed-flow impeller is open with the tip clearance of $0.002 R_{T2}$, where R_{T2} is the radius of the blade tip at the impeller outlet. It has four blades. A comprehensive CFD analysis of the pump has been done for both configurations. Because there is some difference between the optimal flow coefficients of both versions (about 7%), we refer in this article to the relative flow rate ϕ/ϕ_{BEP} , where ϕ_{BEP} is the flow coefficient at the best efficiency point.

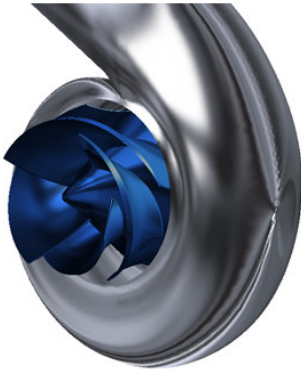


Fig. 1 Model of pump with volute

The available measurements (Fig. 3) show the peak of the noise as well as the vibrations at about 70% of ϕ_{BEP} , which is inside the typical allowable operating range of the pump. These vibrations and noise can be found at rather high NPSH values, but they are very strong especially close to the NPSH value equal to NPSH3. The minimum value of the vibrations and noise appears at the flow coefficient about 117% of ϕ_{BEP} . This corresponds well with the $NPSH_i(\phi)$ curve (Fig. 4), which is very similar for both pump configurations and reaches its

maximum at the flow coefficient of 70% of ϕ_{BEP} and the minimum value approximately at 108% of ϕ_{BEP} . The measurements of noise and vibrations were performed with the volute pump at the NPSH value of 9 m. This is (with the exception of flow coefficients larger than 121% of ϕ_{BEP}) higher than NPSH3 (Fig. 5), but lower than the NPSHi value. Here NPSH3 is defined as the NPSH required for the 3% drop of the total head of the pump. Therefore it can be expected that the level of the noise and vibrations is closely connected to the cavitation phenomena, which can include (at least at the flow coefficients close to the noise level maximum) the cavitation instabilities with highly unsteady behaviour.

In this study the ANSYS CFX commercial CFD package has been used to solve URANS equations together with the Rayleigh-Plesset model, which is included in the ANSYS CFD software to describe the interphase mass transfer in the framework of the homogenous multiphase model. The two-phase system is solved for the vapour and the liquid with non-condensable gas. Though this cavitation model is based on a highly simplified Rayleigh-Plesset equation for the radius of a spherical cavitation bubble, it is very robust and effective for the analysis of the problems, where the void fraction is highly important in forming flow structures but where the details of the bubble dynamics (especially the collapses and rebounds) are not of primary interest [5].

The SST-SAS turbulence model [19] has been employed to capture the highly unsteady phenomena inside the pump. It represents a good compromise between widely used SST model and LES or DES (Detached Eddy Simulation) models, which are too costly for comprehensive turbomachinery applications. The authors of this paper have already used the SST-SAS model for the simulation of cavitation instability in the backflow vortices in front of an inducer (running at the NPSH values close to NPSH3) with fairly good results [20], better than those obtained with the RSM and EARSM turbulence models.

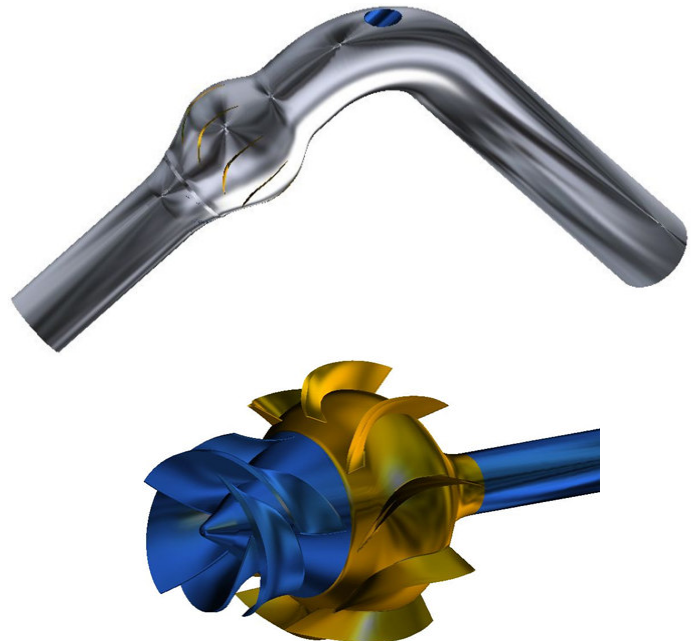


Fig. 2 Model of pump with axial diffuser and elbow

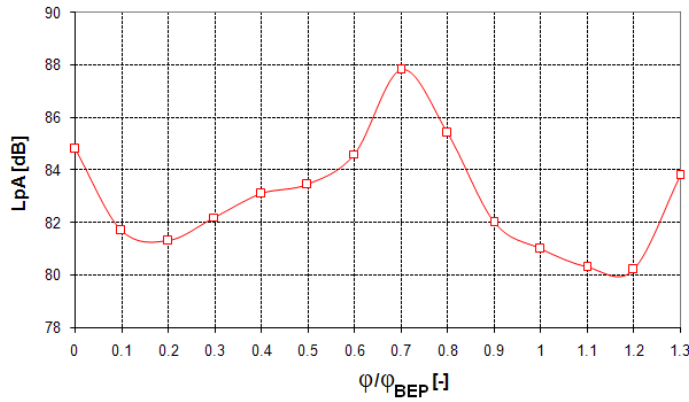


Fig. 3 Measured noise emissions. Pump with volute

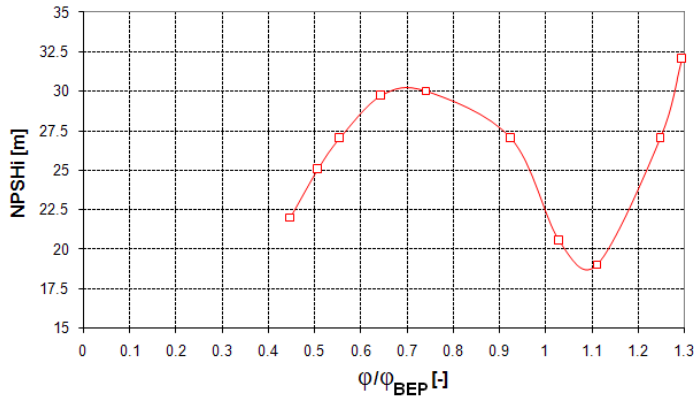


Fig. 4 Cavitation inception at different flow coefficients. Pump with volute. CFD

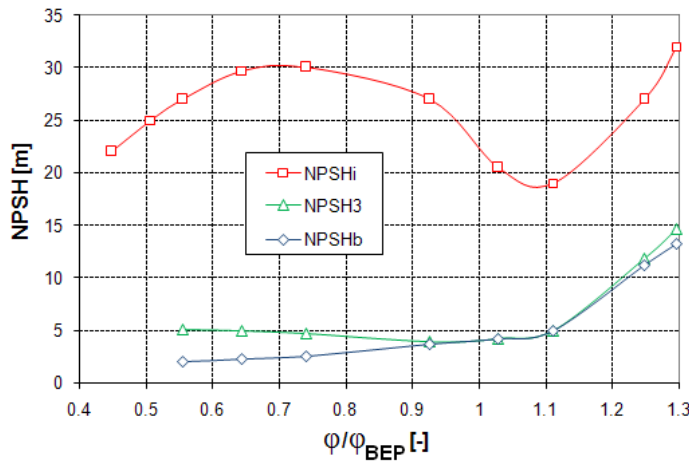


Fig. 5 Curves of NPSH required for cavitation inception, 3% drop of pump total head and cavitation breakdown. Pump with volute. CFD

The computational grids represent approximately 2 mil. grid nodes for both pump models. Fully transient calculations were applied with the time step chosen according to the angular speed Ω ; there are 180 time steps during one shaft revolution, which means that every time step the rotor rotates by 2 degrees. With such a time step three inner coefficient loops per step are sufficient to reach a convergent solution.

3. CFD ANALYSIS OF THE OVERALL CAVITATION PERFORMANCE OF PUMPS

As it was mentioned in the previous chapter, we can expect, that the level of the noise and vibrations is closely connected to the cavitation phenomena. Moreover, these phenomena can depend not only on the flow rate ϕ/ϕ_{BEP} , but also on the NPSH value. For better understanding, figure 5 shows three important cavitation curves: NPSH required for cavitation inception (NPSHi), NPSH required for the 3% drop of the total head of the pump (NPSH3) and NPSH required for the cavitation breakdown (NPSHb). It is important to define how the NPSHi curve was obtained. In practice, there are different criteria when the cavitation inception occurs. They are based either on the static pressure, which has to drop below the saturated vapour pressure on an agreed minimum area, or on the calculated void fraction. We used the second criterion (which seems to be more correct) and required to reach the minimum void fraction of 10%, no matter what the area is. In figure 5 we can see, that close to ϕ_{BEP} curves NPSH3 and NPSHb approach each other, but going to the right (or especially to the left) the difference NPSH3-NPSHb increases. This is caused by a different character of the head-drop curves. Close to ϕ_{BEP} the head-drop curves are very steep at $NPSH = NPSH3$ while at suboptimal flow coefficients the gradient decreases, as we can see in figures 6 - 7 which show the head-drop curves for $\phi/\phi_{BEP} = 1.03$ and $\phi/\phi_{BEP} = 0.64$. In figure 5 we can also see, that for the flow

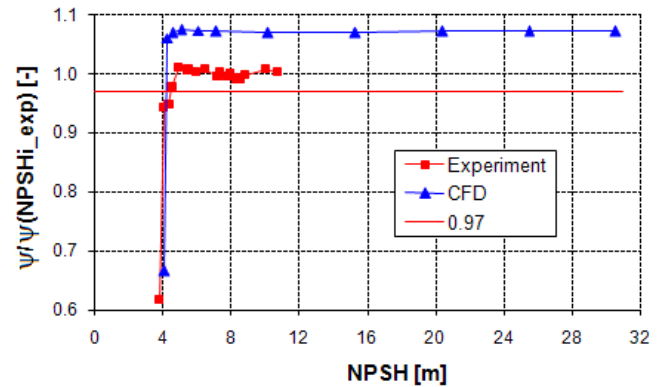


Fig. 6 Head-drop curve for $\phi/\phi_{BEP} = 1.03$. Comparison of CFD analysis and experiment. Pump with volute

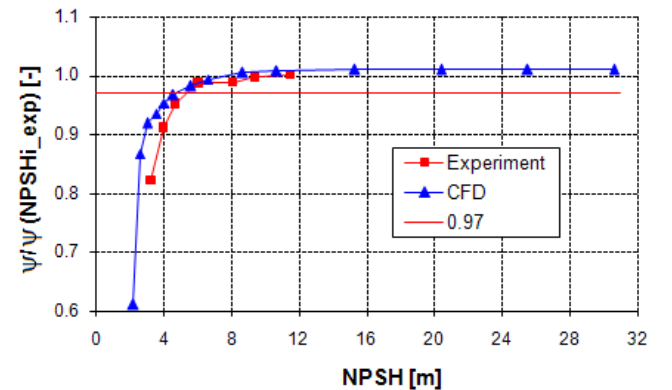


Fig. 7 Head-drop curve for $\phi/\phi_{BEP} = 0.64$. Comparison of CFD analysis and experiment. Pump with volute

coefficients $\phi \geq \phi_{BEP}$ the distance between NPSHi and NPSH3 does not change too much; it is in the range from 14 to 17 m. However for suboptimal flow coefficients the distance rapidly grows and reaches its maximum at about 70% of ϕ_{BEP} .

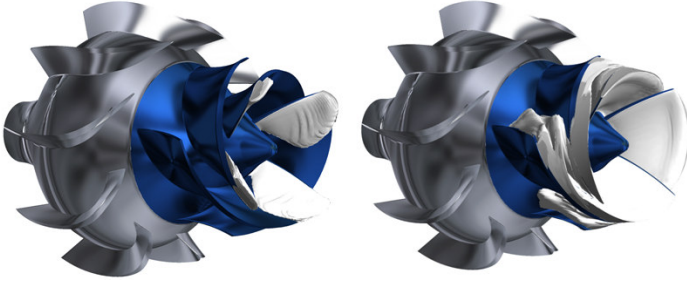


Fig. 8 Regions in the impeller with void fraction over 10%.
Pump with axial diffuser, $\phi/\phi_{BEP}=0.55$.
NPSH \approx NPSH3 (left), NPSH \approx NPSHb (right)

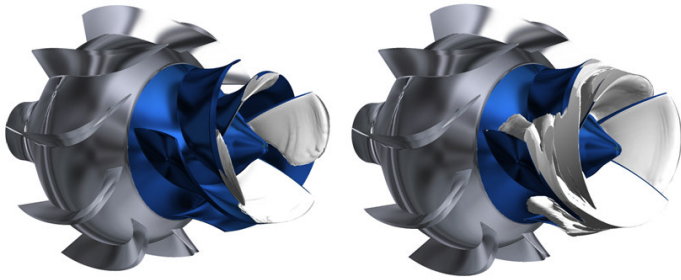


Fig. 9 Regions in the impeller with void fraction over 10%.
Pump with axial diffuser, $\phi/\phi_{BEP}=0.74$.
NPSH \approx NPSH3 (left), NPSH \approx NPSHb (right)

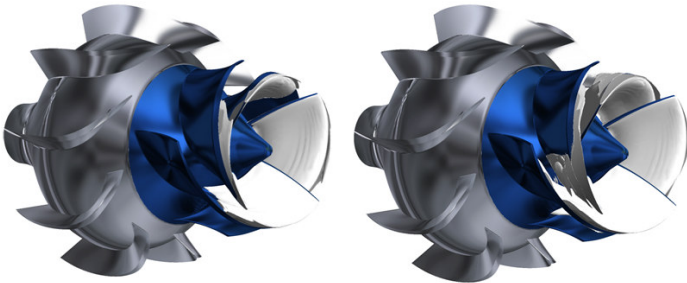


Fig. 10 Regions in the impeller with void fraction over 10%.
Pump with axial diffuser, $\phi/\phi_{BEP}=0.93$.
NPSH \approx NPSH3 (left), NPSH \approx NPSHb (right)

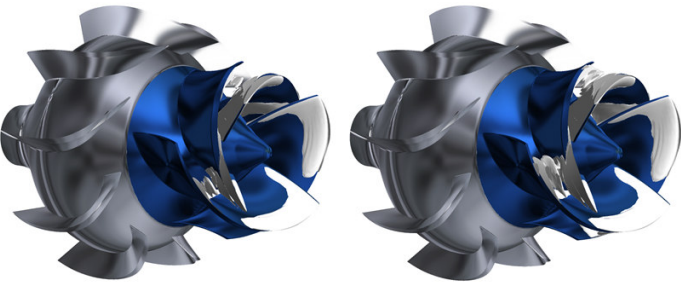


Fig. 11 Regions in the impeller with void fraction over 10%.
Pump with axial diffuser, $\phi/\phi_{BEP}=1.1$.
NPSH \approx NPSH3 (left), NPSH \approx NPSHb (right)

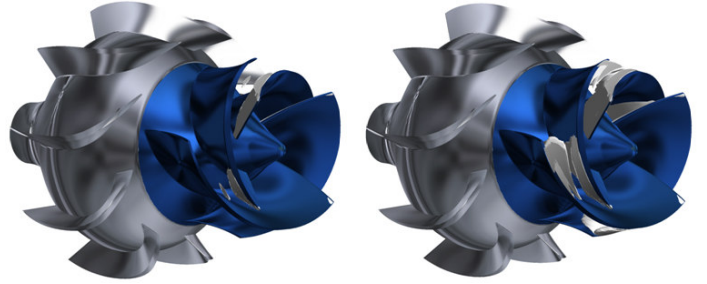


Fig. 12 Regions in the impeller with void fraction over 10%.
Pump with axial diffuser, $\phi/\phi_{BEP}=1.3$.
NPSH \approx NPSH3 (left), NPSH \approx NPSHb (right)



Fig. 13 Regions in the impeller with void fraction over 90%.
Pump with axial diffuser, $\phi/\phi_{BEP}=0.55$.
NPSH \approx NPSH3 (left), NPSH \approx NPSHb (right)

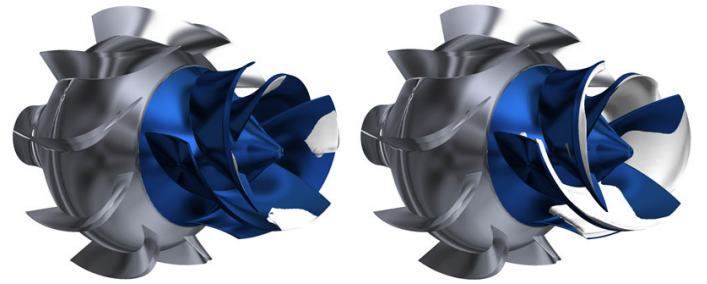


Fig. 14 Regions in the impeller with void fraction over 90%.
Pump with axial diffuser, $\phi/\phi_{BEP}=0.74$.
NPSH \approx NPSH3 (left), NPSH \approx NPSHb (right)

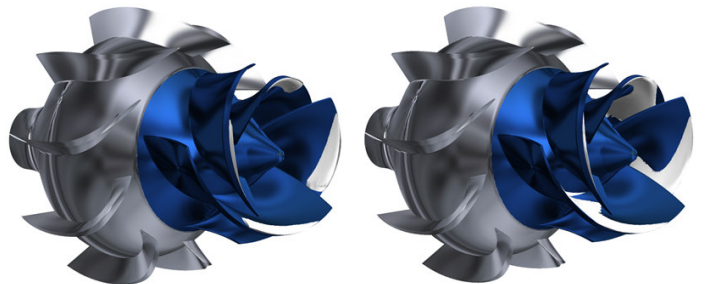


Fig. 15 Regions in the impeller with void fraction over 90%.
Pump with axial diffuser, $\phi/\phi_{BEP}=0.93$.
NPSH \approx NPSH3 (left), NPSH \approx NPSHb (right)

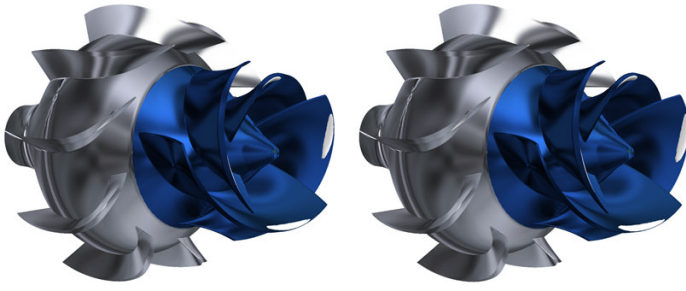


Fig. 16 Regions in the impeller with void fraction over 90%.
Pump with axial diffuser, $\phi/\phi_{BEP} = 1.1$.
NPSH \approx NPSH3 (left), NPSH \approx NPSHb (right)

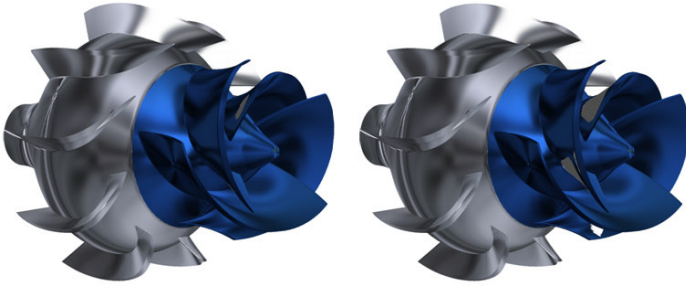


Fig. 17 Regions in the impeller with void fraction over 90%.
Pump with axial diffuser, $\phi/\phi_{BEP} = 1.3$.
NPSH \approx NPSH3 (left), NPSH \approx NPSHb (right)

Next figures show the cavitation regions inside the impeller for different flow rates and two values of NPSH: NPSH3 and NPSHb. We used figures from the pump with the axial diffuser because there is a better insight into the pump. Nevertheless the pictures of cavitation regions inside the impeller of the volute pump do not differ considerably. In fact changes of these regions in time are more visible, so we tried to find some "average" pictures for each flow condition. There are two sets of pictures. Figures 8 - 12 show the isosurfaces, on which the void fraction reaches 10%. This is a numerical equivalent of the experimental visualization of cavitation clouds. Figures 13 - 17 show the isosurfaces, on which the void fraction reaches 90%. In other words, they show cavitation caverns filled with the void fraction only. These caverns behave as the obstacles changing the shape of the blade-to-blade passages of the impeller. As the flow coefficient increases, they are moving from the suction side to the pressure side of the blades.

4. CFD ANALYSIS OF DYNAMIC BEHAVIOUR OF PUMPS DUE TO CAVITATION

Based on the results presented in the previous chapter we decided to perform detailed analysis of the cavitation dynamics at the flow rate $\phi/\phi_{BEP} = 0.7$ for both pump variants. As the measurements of the pressure pulsations and vibrations are available only for the volute pump, most results in this paper are devoted to this one. There are two ways how to present the highly unsteady cavitation phenomena in the pump: prepared videos and frequency analysis. Unfortunately videos are not suitable for documents distributed usually in PDF format, so we have to replace them with only several figures. As far as the frequency analysis is concerned, it is based on the Fast Fourier

Transformation (FFT). To be able to link different frequencies with cavitation phenomena, we analysed first the spectrum of the discharge pressure for the regime with NPSH value greater than NPSHi. The results are shown in figure 18. Here we can see, that the dominant frequency is $4f_\Omega$ (impeller blade frequency). It can be linked to the pressure pulsations created when the trailing edges of the blades pass the volute tongue. We can also find increased amplitudes close to the frequency of $3f_\Omega$ and in the vicinity of the shaft frequency. As far as the amplitudes in the vicinity of f_Ω are concerned, they reflect the fact that the calculated flow inside the impeller passages is not perfectly periodic. The frequency of $3f_\Omega$ corresponds to the periodic changes in the impeller inlet recirculation, which is located close to the blade tips (Fig. 19). Figure 20 shows the frequency spectrum of the discharge pressure for the regime with NPSH equal to 9 m, which is the same value as used during pump measurements. The result does not differ much from the figure 18, only the amplitudes close to the shaft frequency start to separate into two peaks.

The situation is quite different in the case NPSH = NPSH3 (Fig. 21). The dominant frequencies can be found at the values about $0.44f_\Omega$ and $3f_\Omega$ and we can also see the increased amplitude close to the value $1.4f_\Omega$. The lowest frequency $0.44f_\Omega$ can be connected with the cavitation clouds, which separate periodically from the backflow region in front of the impeller.

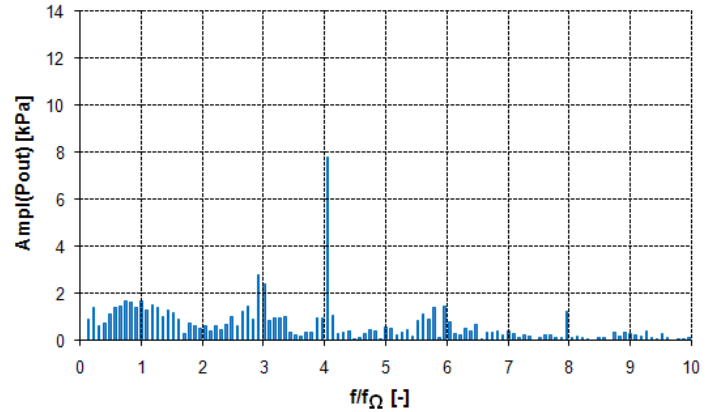


Fig. 18 FFT analysis of discharge pressure. Pump with volute.
 $\phi/\phi_{BEP} = 0.7$, NPSH $>$ NPSHi. CFD analysis

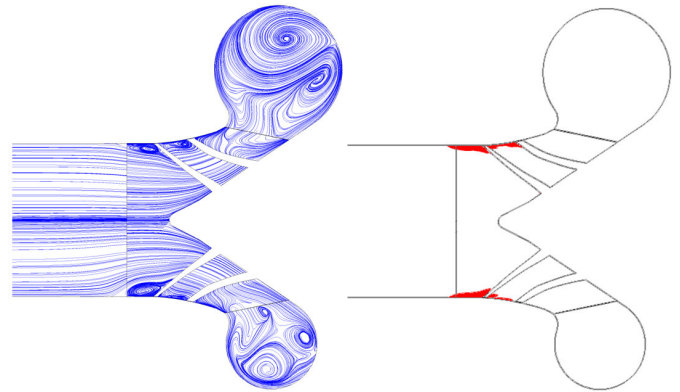


Fig. 19 Meridional cross-section of the pump with volute. CFD.
Meridional streamlines (left) and areas of backflow (red areas on the right). $\phi/\phi_{BEP} = 0.7$, NPSH $>$ NPSHi

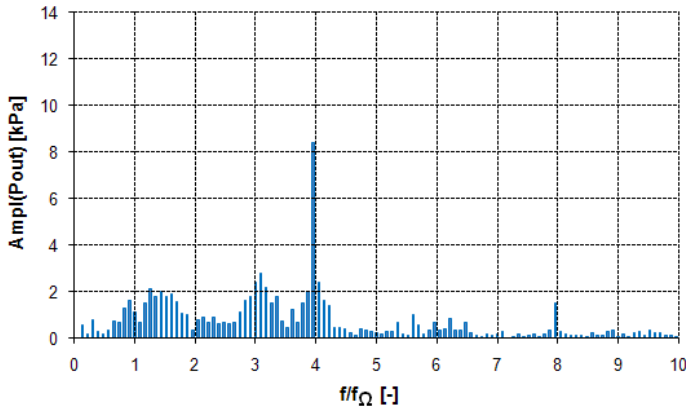


Fig. 20 FFT analysis of discharge pressure. Pump with volute.
 $\phi/\phi_{BEP} = 0.7$, NPSH = 9 m. CFD analysis

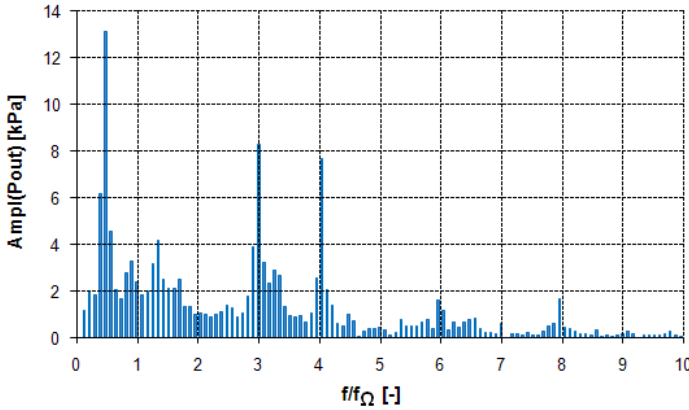


Fig. 21 FFT analysis of discharge pressure. Pump with volute.
 $\phi/\phi_{BEP} = 0.7$, NPSH = NPSH3. CFD analysis

In figure 22 we can see the separation of such cavitation clouds in front of the impeller, which is adjusted in a fixed position. The time interval between two successive pictures represents the rotation of the impeller by 10° . The second frequency which characterizes the changes of cavitation in the backflow region is $3f_\Omega$. It is approximately 7 times higher than the lowest frequency of $0.44f_\Omega$. Another periodic phenomenon which was detected is connected with the cavitation regions on the suction side of the impeller blades. They change their size and shape with the frequency of $1.4f_\Omega$. The changes of the cavitation regions on the suction side of the impeller blades are shown in figure 23. The time interval between two successive pictures represents the rotation of the impeller by 65° .

In the next step we analysed the frequencies for NPSH equal to NPSH_b (Fig. 24). It is interesting that the frequencies of $0.44f_\Omega$ and $3f_\Omega$ are suppressed in this case. We have found that in this regime the cavitation clouds remarkably block the impeller passages and so the backflow in front of the impeller practically vanish (Fig. 25). We can therefore conclude that frequencies of $0.44f_\Omega$ and $3f_\Omega$ are closely linked to the interaction of cavitation and the backflow in front of the impeller.

We have already mentioned that we can compare calculations with the measurements of pressure pulsations and vibrations of the volute pump. Unfortunately the results of the measurements are available only for NPSH3 = 9 m. In figure 26

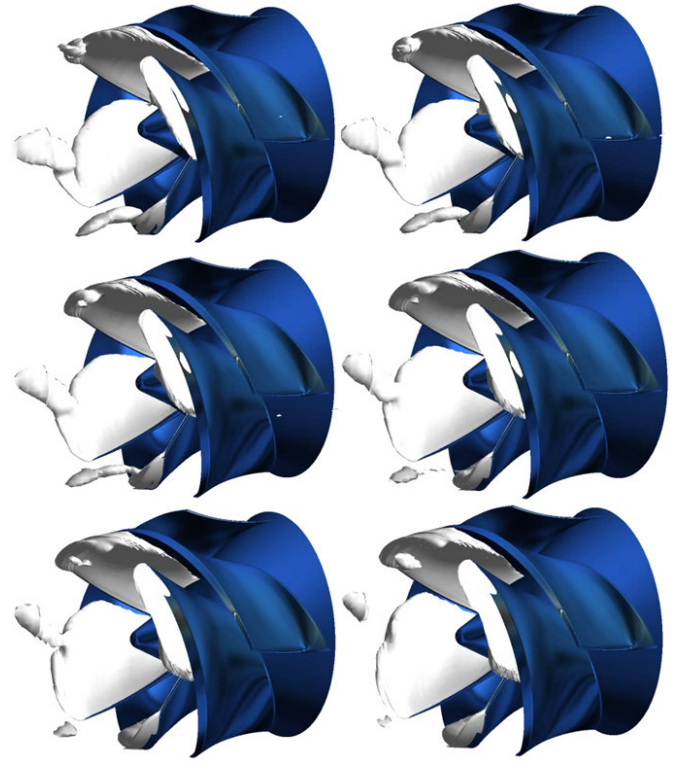


Fig. 22 Cavitation clouds created in backflow vortices.
 $\phi/\phi_{BEP} = 0.7$, NPSH = NPSH3. CFD analysis.
Interval between pictures is 10° of impeller rotation

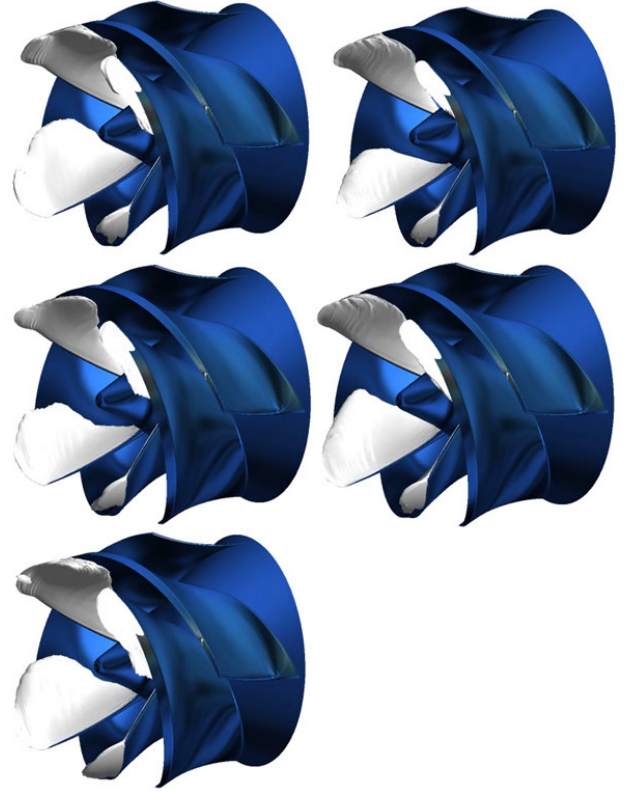


Fig. 23 Changes of cavitation regions on impeller blades.
 $\phi/\phi_{BEP} = 0.7$, NPSH = NPSH3. CFD analysis.
Interval between pictures is 65° of impeller rotation

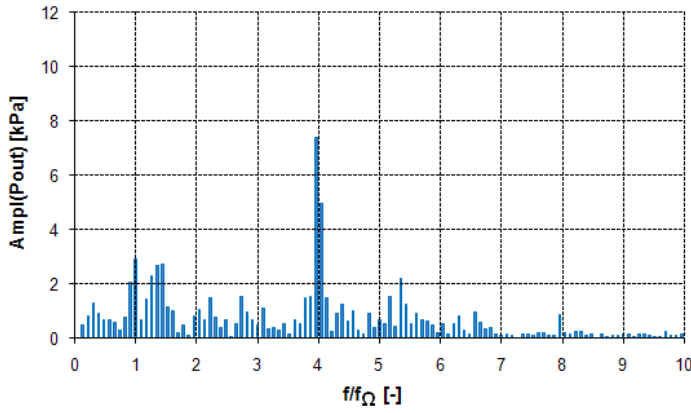


Fig. 24 FFT analysis of discharge pressure. Pump with volute.
 $\phi/\phi_{BEP} = 0.7$, NPSH = NPSHb. CFD analysis

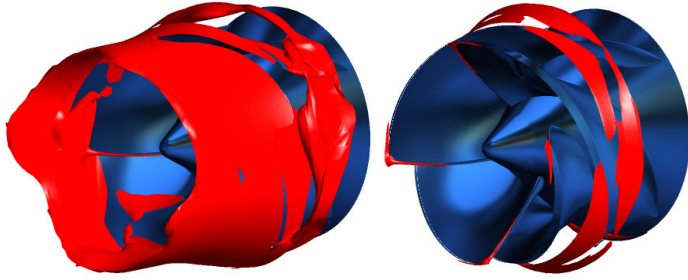


Fig. 25 Backflow in the impeller. Pump with volute.
 $\phi/\phi_{BEP} = 0.7$. NPSH = NPSH3 (left) and NPSHb (right).
CFD analysis

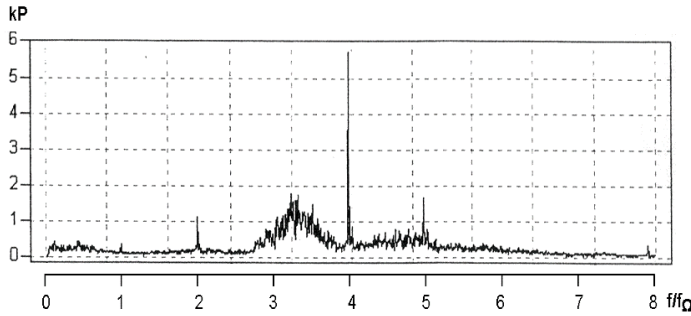


Fig. 26 FFT analysis of discharge pressure. Pump with volute.
 $\phi/\phi_{BEP} = 0.7$, NPSH = 9 m. Experiment

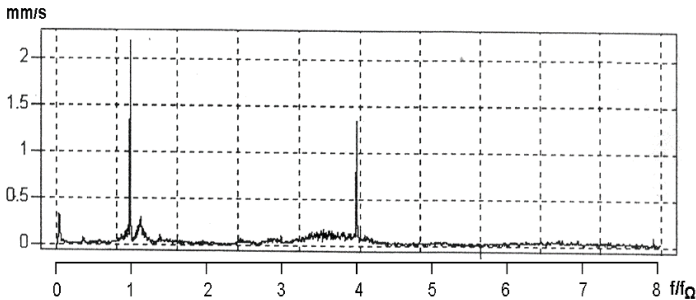


Fig. 27 FFT analysis of vibrations. Pump with volute.
 $\phi/\phi_{BEP} = 0.7$, NPSH = 9 m. Experiment

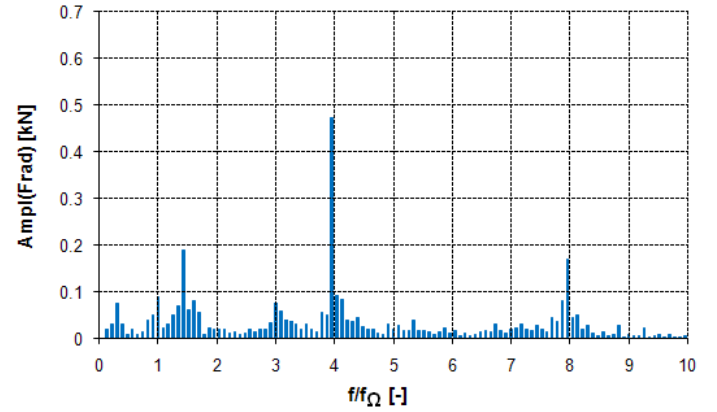
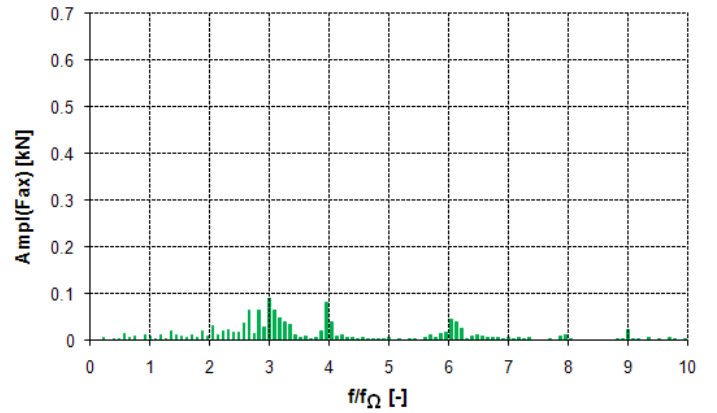


Fig. 28 FFT analysis of forces acting on the impeller.
Pump with volute. $\phi/\phi_{BEP} = 0.7$, NPSH = 9 m. CFD

we can see the FFT analysis of the measured discharge pressure pulsations. There is a dominant frequency of $4f_\Omega$ (impeller blade frequency) and increased amplitudes are also close to the frequency of $3.3f_\Omega$, which is similar to the frequency of $3f_\Omega$ in the CFD analysis. Unlike the calculations, the measurements did not find increased amplitudes in the vicinity of the shaft frequency. Concerning the measured vibrations, they are shown in figure 27. There are two dominant frequencies: the shaft frequency and the impeller blade frequency. We can also find a small peak at the frequency of $1.2f_\Omega$ and increased amplitudes between the values of $3.3f_\Omega$ and $3.7f_\Omega$. As far as the shaft frequency is concerned, we suppose it rises from the mechanical reasons (impeller imbalance and coupling). To compare figure 27 with the CFD analysis we analysed the axial and radial forces acting on the impeller (Fig. 28). The frequency analysis of the radial forces, which are the main source of vibrations, shows three dominant frequencies. The most important is the impeller blade frequency $4f_\Omega$, quite high amplitudes can be found at the frequencies of $1.4f_\Omega$ and $8f_\Omega$. Increased amplitudes can be also found close to the frequencies of $0.44f_\Omega$, f_Ω and $3f_\Omega$. When the value of NPSH drops to NPSH3, the FFT analysis of the calculated radial forces becomes practically unchanged (Fig. 29) while the amplitudes of the axial forces change dramatically, especially close to the frequencies of $0.44f_\Omega$ and $3f_\Omega$.

We also tried to compare the FFT analysis of the calculated discharge pressure pulsations as well as the forces acting on the impeller of the volute pump and the pump with the axial diffuser. The results are very similar with exception of the

impeller blade frequency $4f_\Omega$, which practically disappears. It can be seen e.g. from figures 29 - 30 showing the FFT analysis of the forces acting on the impeller of both pump configurations at the same flow conditions.

5. CONCLUSIONS

The presented CFD analysis has provided a good picture of the cavitation structures inside the pump and their dynamics for a wide range of flow coefficients and NPSH values, which would be very difficult and expensive to obtain through the experimental research. Cavitation instabilities were detected at the flow rate of $0.7\phi_{BEP}$ close to the NPSH3 value. The frequencies of $0.44f_\Omega$ and $3f_\Omega$ are closely linked to the interaction of cavitation and the backflow in front of the impeller. The frequency of $1.4f_\Omega$ is connected with the cavitation regions on the suction side of the impeller blades. They change their size and shape, as shown in figure 23. The calculated cavitation performance $\psi(\phi, NPSH)$ has been compared with the available measurements in a closed horizontal plane loop with a good agreement. The calculated results and their frequency analysis also correspond fairly well to the measured noise, pressure pulsations and vibrations.

In [20] we examined the dynamic behaviour of cavitation phenomena in the suction part of a radial-flow multistage pump with the three-blade inducer. Here the unsteady cavitation in the backflow vortices was obtained with the dominant frequency $f_1 = 0.166 nf_\Omega$, where $n = 3$ is the number of backflow vortices.

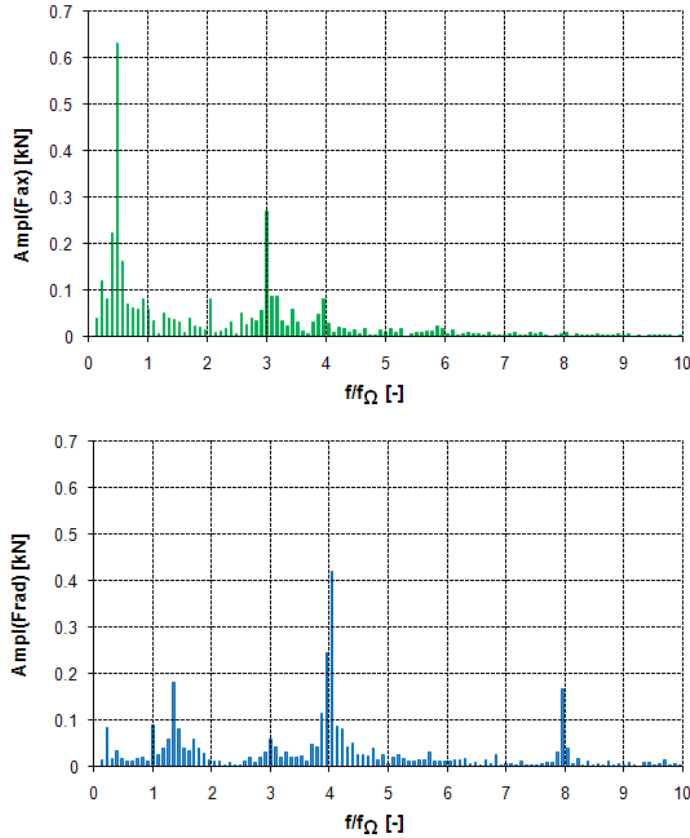


Fig. 29 FFT analysis of forces acting on the impeller.

Pump with volute. $\phi/\phi_{BEP} = 0.7$, NPSH = NPSH3. CFD

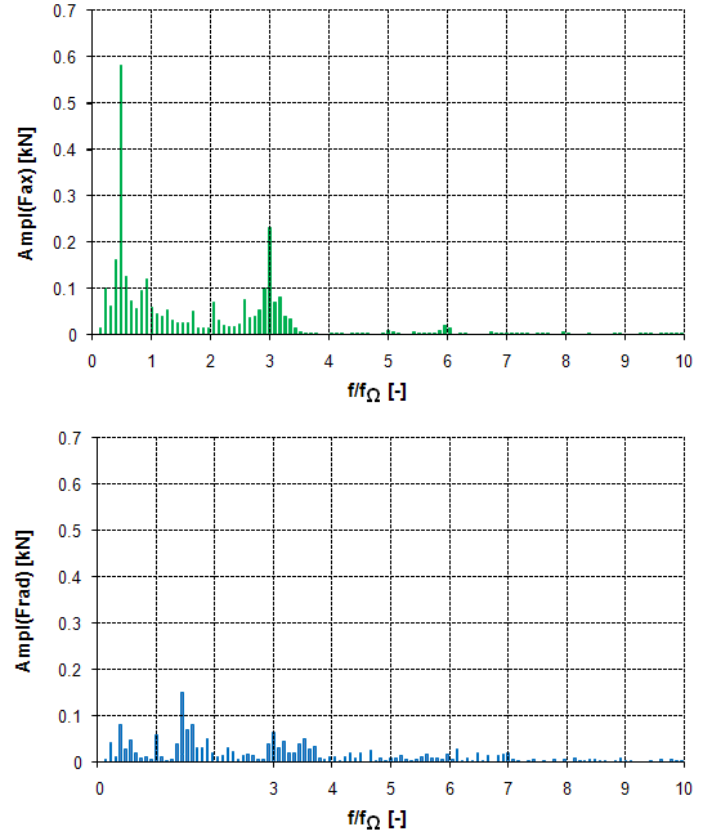


Fig. 30 FFT analysis of forces acting on the impeller.

Pump with axial diffuser. $\phi/\phi_{BEP} = 0.7$,
NPSH = NPSH3. CFD analysis

This corresponded well with the observations by Tsujimoto [14] who measured the dominant frequency $f_1 = 0.16 nf_\Omega$, $n = 5$ in the three-blade inducer. We concluded that URANS based models of turbulence (including the SST-SAS model) were not able to predict the number of backflow vortices different from the number of inducer blades. The same is valid in this study concerning cavitating flow in the mixed-flow pump. We could detect four vortices separating periodically in the backflow region. So the dominant frequency $0.44f_\Omega$ can be written this way: $f_1 = 0.11 Z_1 f_\Omega$, where $Z_1 = 4$ is the number of the impeller blades.

The FFT analysis of the calculated discharge pressures and forces is based on the dataset of 2048 timesteps, which represents about 11.4 impeller revolutions. About ten more impeller revolutions were necessary to obtain initial periodic solution. It requires quite large CPU times for every value of NPSH. It can be seen from the graphs of the FFT analysis that 2048 timesteps are not enough to get a really fine resolution of the frequencies and corresponding amplitudes. Also those ten initial revolutions may be insufficient to provide a perfectly periodic solution and that is why the lowest calculated frequencies can be influenced by the computational reasons. Nevertheless the amplitudes corresponding to the frequencies of $0.44f_\Omega$, $1.4f_\Omega$ and $3f_\Omega$ (regime $\phi/\phi_{BEP} = 0.7$, NPSH = NPSH3) are high enough to be linked to the cavitation and flow phenomena, not to the numerical errors. The experimental verification and visualization is nevertheless planned in the close future.

ACKNOWLEDGMENTS

This work has been supported by the Department of Industry and Trade of the Czech Republic under grant FR-TII/418 "Research and Development of High-Speed Pumps with Suppressed Cavitation".

REFERENCES

- [1] Os, M.J., Op de Woerd, J.G.H and Jonker, J.B. (1997), *A Parametric Study of the Cavitation Inception Behaviour of a Mixed-Flow Pump Impeller Using a Three-Dimensional Potential Flow Model*. Proc. ASME FEDSM97-3374.
- [2] Nagahara, T., Sato, T and Okamura, T. (2001), *Effect of the Submersed Vortex Cavitation Occurred in Pump Suction Intake on Hydraulic Forces of Mixed Flow Pump Impeller*. CAV2001:sessionB8.006, pp. 1-8.
- [3] Sedlar, M. (2001), *Numerical Investigation of Flow in Mixed-Flow Pump with Volute*. TASK QUARTERLY 5, No. 4, pp. 595-602.
- [4] Sedlar, M., Marsik, F. and Safarik, P. (2002), *Numerical Analysis of Cavitated Flows in Mixed-Flow Pump Impellers*. Proc. Proc 3rd Int. Conference on Transport Phenomena in Multiphase Systems, Heat 2002, pp. 461-466.
- [5] Sedlar, M., Zima, P. and Muller, M. (2009), *CFD Analysis of Cavitation Erosion Potential in Hydraulic Machinery*. Proc. 3rd IAHR WG Meeting 2009, pp. 205-214.
- [6] Oh, H.W. (2010), *Design Parameter to Improve the Suction Performance of Mixed-Flow Pump Impeller*, Proc. IMechE Vol. 224, Part A: J. Power and Energy, JPE986, pp. 881-887.
- [7] Harada, I., Kobayashi, K. and Ono, S. (2010), *Prediction of Axial Thrust for Mixed-Flow Pumps with Vaned Diffuser by Using CFD*. Int. Journal of Fluid Machinery and Systems, Vol. 3, No. 2, pp. 160-168.
- [8] Kobayashi, K. and Chiba, Y. (2010), *Computational Fluid Dynamics of Cavitating Flow in Mixed Flow Pump with Closed Type Impeller*. Int. Journal of Fluid Machinery and Systems, Vol. 3, No. 2, pp. 113-121.
- [9] Yamamoto, K. and Tsujimoto, Y. (2009), *Backflow Vortex Cavitation and Its Effects on Cavitation Instabilities*. Int. Journal of Fluid Machinery and Systems, Vol. 2, No. 1, pp. 40-54.
- [10] Kamijo, K., Shimura, T. and Watanabe, M. (1977), *An Experimental Investigation of Cavitating Inducer Instability*, ASME Paper 77-WA/FW-14.
- [11] Tsujimoto, Y., Yoshida, Y., Maekawa, M., Watanabe, S. and Hashimoto, T. (1997), *Observations of Oscillating Cavitation of an Inducer*. ASME Jour. Fluids Engng. , 119, No. 4, pp. 775-781.
- [12] Brennen, C.E. (1994), *Hydrodynamics of Pumps*. Concepts Eti & Oxford University Press.
- [13] Tsujimoto, Y., Kamijo, K. and Yoshida Y. (1993), *A Theoretical Analysis of Rotating Cavitation in Inducers*. ASME Jour. Fluids Engng., 115, No. 1, pp. 135-141.
- [14] Tsujimoto, Y. (2006), *Cavitation Instabilities in Inducers*, Design and Analysis of High Speed Pumps, Educational Notes RTO-EN-AVT-143, Paper 8, pp. 8-1 - 8-26.
- [15] Berntsen, G., Kjeldsen, M. and Muller, R. (2001), *Cavitation Induced Dynamics in Hydraulic Machinery*, Proc. 10th IAHR WG Meeting on the Behaviour of Hydraulic Machinery under Steady Oscillatory Conditions, pp. 1-8.
- [16] Bouziad, Y.A. (2005) *Physical Modelling of Leading Edge Cavitation: Computational Methodologies and Application to Hydraulic Machinery*, Ecole Polytechnique Federale de Lausanne, Thesis No. 3353.
- [17] Tsujimoto, Y. (2005), *Tip Leakage and Backflow Vortex Cavitation*, Proc. CISM Advanced School on Fluid Dynamics of Cavitation and Cavitating Turbopumps.
- [18] Tsujimoto, Y., Horiguchi, H. and Yonezawa, K. (2010), *Cavitation Instabilities in Turbopump Inducers. Analyses in 1-3 Dimensions*. Int. Journal of Fluid Machinery and Systems, Vol. 3, No. 2, pp. 170-180.
- [19] Menter, F.R., Kuntz, M. and Bender, R. (2003), *A Scale-Adaptive Simulation Model for Turbulent Flow Prediction*. AIAA paper 2003-0767.
- [20] Sedlar, M., Bajorek, M. and Soukal, J. (2007), *Investigation of Cavitation Phenomena in Suction Part of Radial-Flow Pump*. Proc. 7th European Conference on Turbomachinery, pp. 785-794.

Cavitation modelling using RANS approach

A.I.Oprea / Wartsila Netherlands

N.Bulten / Wartsila Netherlands

Iulia.Oprea@wartsila.com

Norbert.Bulten@wartsila.com

ABSTRACT

The use of cavitation modeling within the maritime industry area is in a crucial state. The advances in the computer power, the understanding of the numeric's and of the cavitation phenomena do make possible to bring these kinds of simulations into the daily use. The goal is a cavitation method to be applied from the design stage to the problem solving situations.

The paper will present cavitating results obtained for a two-dimensional case: NACA 0015 profile and for a three-dimensional case: Twist11 foil. These cases are the most popular numerical and experimental benchmarks used to validate the cavitation simulations. This step will prove the capability of simulations when using the proposed cavitation modeling and RANS solver approach. For an adequate mesh and proper turbulence modeling, predictions for developed cavitation regions like: sheet, clouds or vortices are possible.

In a final step, the cavitation modeling will be put to the test for a real application challenge: a propeller. This last complex case will involve a rotating propeller and therefore moving mesh approach has to be implemented as well.

By the end of the paper, the proposed cavitation method used within a RANS code for dedicated flow features grids, proves to give consistent results.

NOMENCLATURE

<i>Symbol</i>	<i>Definition</i>	<i>(unit)</i>
c	Chord length	(m)
C _d	Drag coefficient	(-)
C _l	Lift coefficient	(-)
C _p	Pressure coefficient	(-)
n ₀	Number of seed bubbles	(-)
p	Pressure	(Pa)
p _v	Vapor pressure	(Pa)
R	Bubble radius	(m)
S	Span	(m)
S _{av}	Source of vapor volume fraction	(1/s)
t	Time	(s)
u	velocity	(m/s)
V _v	Fraction of control volume V	(-)
α	Volume fraction	(-)
α _v	Volume fraction of vapor	(-)
μ	Dynamic Viscosity	(Pa·s)
ρ	Density	(kg/m ³)
σ	Cavitation number	(-)

K _t	Thrust coefficient	(-)
K _q	Torque coefficient	(-)
n	number of rotations per second	(-)
RPM	number of rotations per minute	(-)
D	propeller diameter	(m)
J	advance ratio	(-)
V _{ad}	propeller advance velocity	(m/s)

1. INTRODUCTION

During the last years the usage of the so-called transient moving-mesh simulations in RANS CFD calculations has become more and more common. Due to developments in hardware and software the required calculation times are well within commercially acceptable limits. The application of the fully transient calculation method has lead to interesting new insights.

A second interesting development is the implementation of a cavitation model in the daily CFD work. The cavitation model as used within Wärtsilä has been validated and fine-tuned with the aid of experimental data of a twisted 3D-foil. Excellent agreement of the physical phenomena, like the shape of the cavity and the shedding frequency of the cavity has been found for the foil.

In this paper, results of the wetted and cavitating flow of an open propeller unit are presented.

2. NUMERICAL BACKGROUND

The commercial code Star-CD version 4.02 [1] is used for all flow simulations. The equations for the description of the flow and the modelling of the cavitation are presented in this paragraph. In the present paper the numerical approach used for flow simulations are the incompressible RANS equations. In this case, the system of equations is formed by the mass conservation equation (1) and impulse conservation equations (2).

$$\nabla \cdot \vec{u} = 0 \quad (1)$$

$$\rho \frac{\partial \vec{u}}{\partial t} + \rho \vec{u} \nabla \cdot \vec{u} = -\nabla p + \mu \nabla^2 \vec{u} + \rho \vec{g} \quad (2)$$

In the conservation equations u is the velocity tensor, ρ is fluid density, p is the pressure, g is the gravitational acceleration and μ is the dynamic viscosity of the fluid.

The turbulence models used is a two-equation modified RNG $k-\epsilon$ turbulence model in conjunction with the algebraic law-of-the-wall approach.

The modification / correction of the RNG turbulence model is applied only at the liquid-vapour mixture interface as described and recommended by Reboud [2]. The correction consists in modifying the turbulence viscosity equation only in the mixture region. In turbulent viscosity equation (3), density is defined as in equation (4).

$$\mu_t = f_\mu \rho C_\mu \frac{k^2}{\epsilon} \quad (3)$$

$$f(\rho) = \rho_v + \frac{(\rho - \rho_v)^n}{(\rho_l - \rho_v)^{n-1}} \quad (4)$$

In equation (4), $n=10$ as recommended by Reboud et al.[2], when density is within the mixture region: $\rho_v \leq \rho \leq \rho_l$.

The modified turbulence viscosity equation affects the cavitating simulations, the wetted flow simulations are not influenced by this correction.

The discretization schemes are second order MARS in space and first order Euler implicit in time. For the wetted calculations a steady-state solver procedure is used. For the cavitating conditions and fully transient moving mesh calculations a transient flow calculation, based on the SIMPLE method, is applied.

The implemented cavitation modelling as used for the following simulations is described next. The solution methodology used can handle cavitating flows and belongs to the class of so-called interface-capturing or fixed-grid methods, also known as Volume-of-Fraction (VOF) methods. It deals with a single continuum whose properties vary in space according to its composition. The solution of the transport equations for the component fluids determines the composition.

The transport of vapour is computed according:

$$\frac{\partial \alpha_v}{\partial t} + \nabla \cdot (\alpha_v u) = S_{\alpha_v} \quad (5)$$

In equation (5) S_{α_v} represents the source of volume fraction of vapor. And the volume fraction of vapor is defined as: $\alpha_v = \frac{V_v}{V}$.

Where, V_v is the fraction of the control volume V occupied by vapor.

The initial volume fraction of vapor is defined by the number of seed bubbles n_0 and their initial radius R by:

$$\alpha_v = \frac{(4/3\pi R^3)n_0}{1 + (4/3\pi R^3)n_0} \quad (6)$$

The source term in equation (5) is defined as:

$$S_{\alpha_v} = \frac{4\pi R^2 n_0}{1 + (4/3\pi R^3)n_0} \frac{dR}{dt} \quad (7)$$

In equation (7) the rate of change of a bubble radius is estimated using a simplified Rayleigh-Plesset equation:

$$\frac{dR}{dt} = \text{sign}(p_v - p) \sqrt{\frac{2|p_v - p|}{3\rho_L}} \quad (8)$$

Where p_v is the saturation pressure, p is the local pressure around the bubble and ρ_L is the fluid density. The equation (7) is known as the Rayleigh cavitation model as from Star-CD [1].

The volume fraction of the components is determined from the condition:

$$\alpha + \alpha_v = 1 \quad (9)$$

The properties of the effective fluid vary in space according to the volume fraction of each component. Density is defined by:

$$\rho = \alpha\rho_l + \alpha_v\rho_v \quad (10)$$

and viscosity:

$$\mu = \alpha\mu_l + \alpha_v\mu_v \quad (11)$$

All the transport equations are the same for the effective fluid as in the single phase flow case, with the exception that density and viscosity vary sharply across the cavity surface.

3. BENCHMARK TEST CASES

3.1 2D TEST CASE: NACA0015

Numerical modeling of cavitating flows is difficult, due to the coexistence of two fluids: water and vapor. The main issues are the treatment of the surface between the two phases and the mass transfer from one phase to another. Therefore as a starting point, a simple 2D test case is used first in most of the cavitation assessments.

The cavitation model described previous section is applied for all the cavitating conditions presented in this paper.

A NACA0015 profile is used as 2D test case for the wetted and cavitating flow simulations. Since this is a numerical benchmark test case for many researchers, results are available for comparison purposes, see also Arndt et al. [3] for 3D measurements over NACA0015 foil.

The analyzed NACA0015 profile (see Abbot and Doenhoff [4]) has a chord length of 200 mm and it has been set at an angle of attack of 6 degrees. The domain size is 1400 x 570 mm, divided in 2 chords at the inlet and 4 at the outlet. The profile mesh is a multi-block structured grid, with an O-grid type around the profile, including a small round trailing edge. This structured mesh ensures good control over the y^+ values. A part of the mesh is shown in Figure 1.

The applied boundary conditions are the following: an inlet boundary type with inlet velocity of 6 m/s and a turbulence intensity of 1%, at the outlet a pressure boundary and at the outer domain side walls with slip boundary condition.

Two flow conditions are analyzed: (a) wetted flow and (b) cavitating case at cavitation number $\sigma=1.0$, which should result in a shedding cavity. In the computations a density of 998 kg/m^3 for water and 0.023 kg/m^3 for the vapor is applied. These values correspond with a water/vapor temperature of 24 degrees.

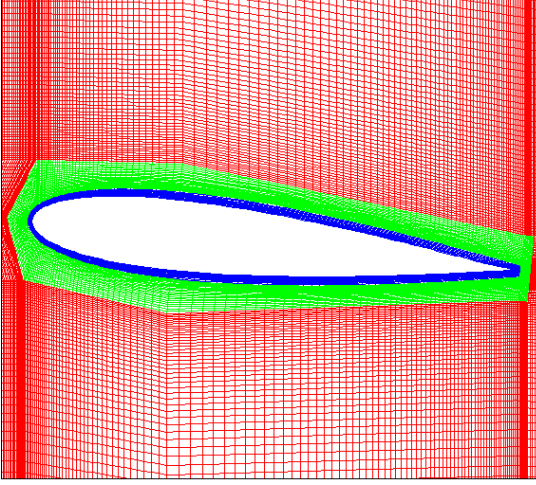


Figure 1: O-grid around NACA0015 profile

3.1. (a) Wetted Flow Results

First the results of the wetted flow RANS calculations are analyzed. The pressure coefficient distribution is shown in Figure 2 where C_p is defined by equation:

$$C_p = \frac{p}{\frac{1}{2} \cdot \rho \cdot u^2} \quad (12)$$

The pressure coefficient value at the stagnation point should be 1.0, based on the analytical solution. In RANS simulations the pressure coefficient can be over-predicted due to the turbulence modeling, see Bulten and Oprea [5]. The current results, based on the RNG k- ϵ turbulence model, give a quite good pressure coefficient value of 1.016 with 1.6% deviation from the analytical value.

Lift (L) and drag (D) of the profile section are expressed in non-dimensional coefficients by equations (13) and (14).

$$C_L = \frac{L}{\frac{1}{2} \rho u^2 c S} \quad (13)$$

$$C_D = \frac{D}{\frac{1}{2} \rho u^2 c S} \quad (14)$$

The results of the CFD calculations are compared with experimental data in the Table 1. The numerical results deviate less than 1% from the experiments. The wetted flow results confirm the accuracy of the method and validation of the 2D wetted flow results.

	CFD	Experiment
Lift	0.667	0.658
Drag	0.014	0.014

Table 1: Lift and Drag, NACA0015

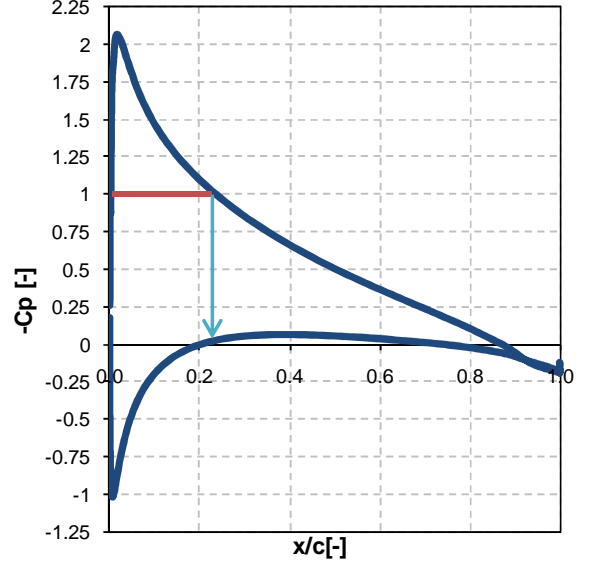


Figure 2: C_p distribution on NACA0015 profile

3.1. (b) Cavitating Flow Results

At this stage, the cavitation model is enabled and time dependent RANS simulations are performed for the 2D NACA0015 profile. Starting from the Bernoulli equation, the cavitation number is defined by equation:

$$\sigma = \frac{p_0 - p_v}{\frac{1}{2} \cdot \rho \cdot u^2} \quad (15)$$

From equation (12) and (15) the relation between pressure coefficient and cavitation number becomes:

$$\sigma = -C_{p \min} \quad (16)$$

For the cavitating condition, the same angle of attack and inflow conditions will be used as for the wetted flow case. The cavitation number value is chosen at 1.0 in order to obtain a clearly present cavity. Based on the wetted flow as shown in Figure 2, a region covering about 25% of the chord length is found to be below sigma of 1.0. These types of cavities are expected to show a non-stable behavior. Therefore this 2D-case is a good preparation step for the more complex 3D shedding cavitating case.

In agreement with the expectations, the results of the calculations showed the non-stable behavior of the cavity. A periodic shedding solution has been found. Results of the variation of the cavitation volume in time are presented in Figure 3 for one period. Analysis of the cavity volume has been used to assess the convergence and shedding period of this 2D transient simulation case.

The averaged cavity shedding period over a larger number of cycles is about 0.06 seconds, resulting in a frequency of about 17Hz. This result is very well in agreement with measurements performed by Arndt et al. [2], which indicates a model tests frequency equal to 18Hz. Simulations results in the literature for

the NACA0015 cavitating profile, are reported by Koop [6] with frequencies varying from 11Hz to 24Hz.

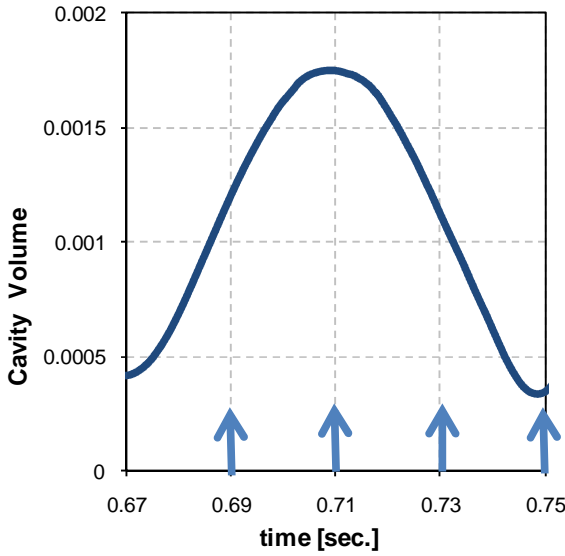


Figure 3: Cavity volume variation on 2D NACA0015 profile at $\sigma = 1.0$

Based on the cavity volume variation as shown in Figure 3, four time steps have been selected for analysis of the vapor concentration. The cavitation contour variation (CAV) and velocity vectors are shown in Figure 4 for $t=0.69s$, $t=0.71s$, $t=0.73s$ and $t=0.75s$ from top to bottom.

These pictures show the vapor concentrations at a certain cross-section in the domain, whereas the cavitation volume is based on the complete numerical domain. It should be noted that the time, giving minimum cavity volume in Figure 3 may not show the lowest vapor concentrations in the contour plots of Figure 4.

At 0.69s, a small leading edge cavity is observed, while at the same time shedding cavity clouds of the previous period are downstream of the foil leading edge.

At 0.71 seconds, the leading edge cavity is increased and the re-entrant jet starts to form; furthermore the cavity clouds from the previous step traveled more downstream.

At 0.73 seconds, the leading edge cavity starts to redraw towards the profile nose, while the clouds start to shed downstream.

At 0.75 seconds, the leading edge cavity disappears while just a few vapor clouds are visible. In a next step, at 0.77 seconds, the leading edge cavity starts to grow and the cycle repeats itself from the 0.69s.

This cavity shedding patterns are confirmed by experiments and simulations in [2] and [6].

The method is therefore successfully applied to the 2D NACA0015 case and the 3D Twist-11 foil case is analyzed and validated in the following.

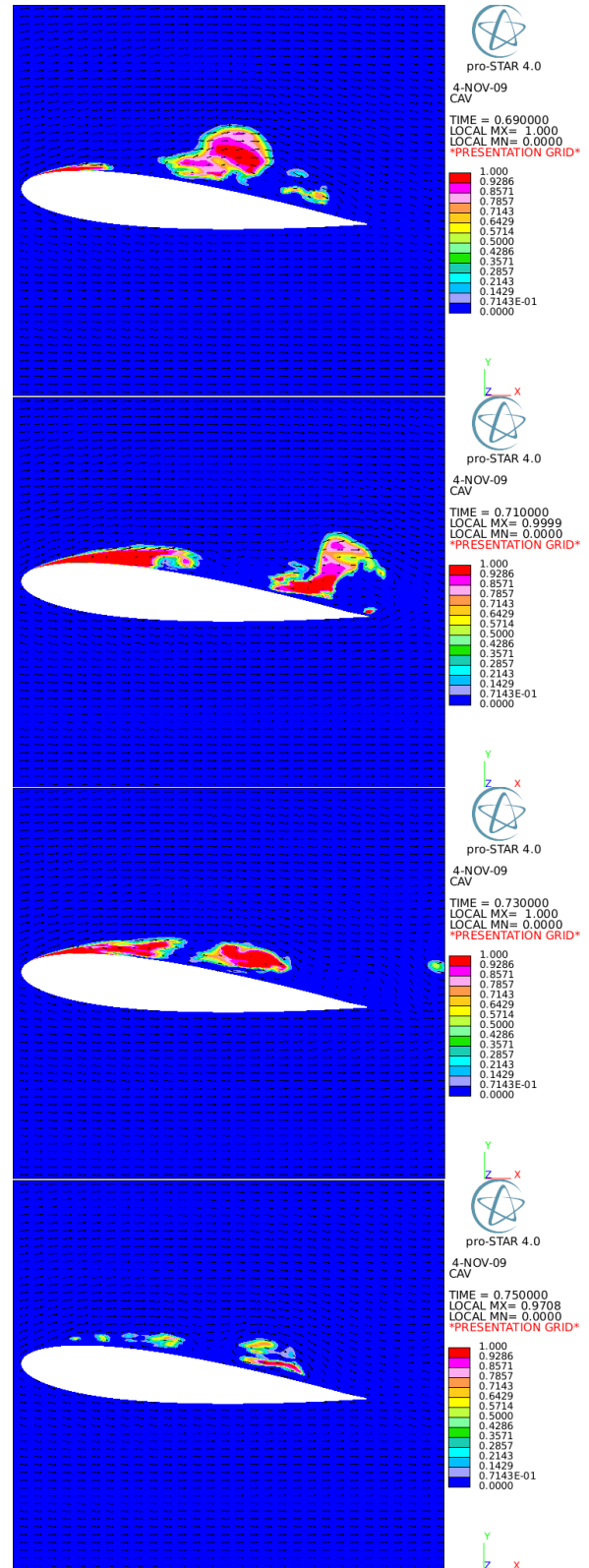


Figure 4: Cavity contours for 2D NACA 0015 profile at 0.69s, 0.71s, 0.73s and 0.75s, from top to bottom

3.2 3D TEST CASE: TWIST-11 FOIL

The Twist-11 foil test case is a special designed geometry to produce a complex 3D cavity at the mid-chord of the hydrofoil, which forms and detaches periodically. The hydrofoil profile is the NACA0009 foil, see Abbot and Doenhoff [4] for details. To obtain a localized low pressure zone at the mid-span of the foil, the angle of attack is increasing from -2 degrees at the tunnel walls to 9 degrees in the middle of the foil.

The measurements of the foil were performed at the Delft University of Technology water tunnel explained by Foeth in [7] and Foeth and van Terwisga [8]. The test section dimensions are 300 mm x 300 mm, with a length of 600 mm. As recommended in the VIRTUE project [9], the length of the computational domain is 7 chord lengths, two ahead of the profile and 4 behind the trailing edge. Also, the mesh approach for the 3D Twist-11 is similar with the NACA0015, a multi-block structured grid, with an O-grid type around the profile extended on the span-wise direction with an angle of attack as shown in Figure 5.

The Twist-11 geometry grid has 3 millions cells with about 2 millions cells only within cell blocks in the O-grid and the blocks adjacent to the O-grid, where the cavitation is expected, as seen in Figure 5.

This fine mesh around the foil has the capability to capture small cavity clouds expected to shed from the leading edge cavity, in a similar way as for the NACA0015 2D profile.

Given the numerical domain and mesh as previously described the following boundary conditions are applied. At the inlet a prescribed inlet velocity is used, at the outlet a constant pressure condition, at the tunnel walls a wall boundary with slip condition and at the mid of the foil a symmetry condition. Since only half of the wing is modelled the number of cells is kept to a reasonable number. The RANS equations are solved using an implicit SIMPLE algorithm and second order spatial discretization.

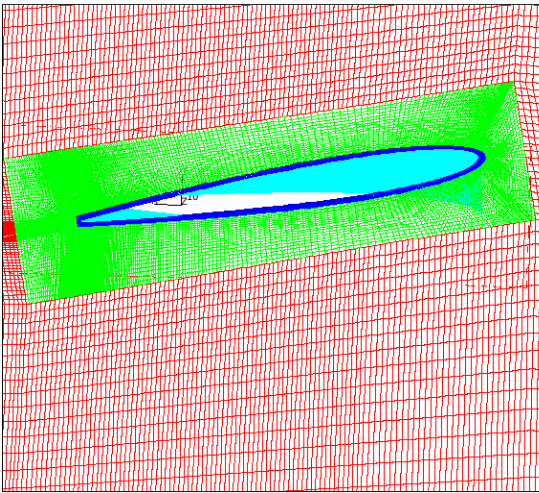


Figure 5: O-grid view of 3D Twist-11 foil

3.2. (a) Wetted Flow Results

The simulation conditions for the Twist-11 foil wetted flow case are as follows: an inlet velocity of 6.75 m/s and an outlet pressure of 97.0 kPa.

In the measurements the Twist-11 foil was equipped with 12 sensor points at 50, 40 and 30 % of the foil span. The comparison of the measured pressure coefficient and the computed values are presented in Figure 6. This figure shows a very good agreement between the measured and simulated pressure coefficient values.

The hydrofoil was also mounted with two components load cells at both tunnel walls to measure the lift on the foil. The measured lift values for different velocities were fitted with the following quadratic relation (17), as from Foeth [10].

$$Lift = 10.052 \cdot u^2 \quad (17)$$

Measured and simulated lift values are shown Figure 7 with good agreement.

It is concluded that the results as shown in Figure 6 and Figure 7 show a good agreement between experiments and simulations for pressure and lift predictions on the Twist-11 foil in the wetted flow case. Consequently, the accuracy of the numerical simulations is sufficiently for further analysis of the flow over the foil.

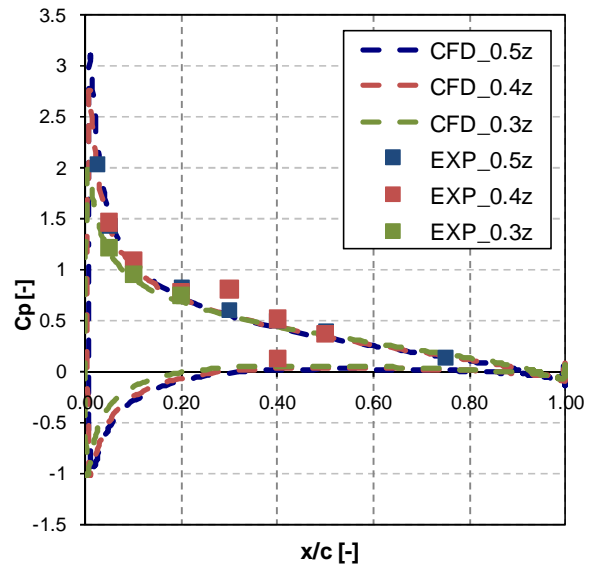


Figure 6: Comparison of measured and calculated Cp over the 3D Twist-11 foil

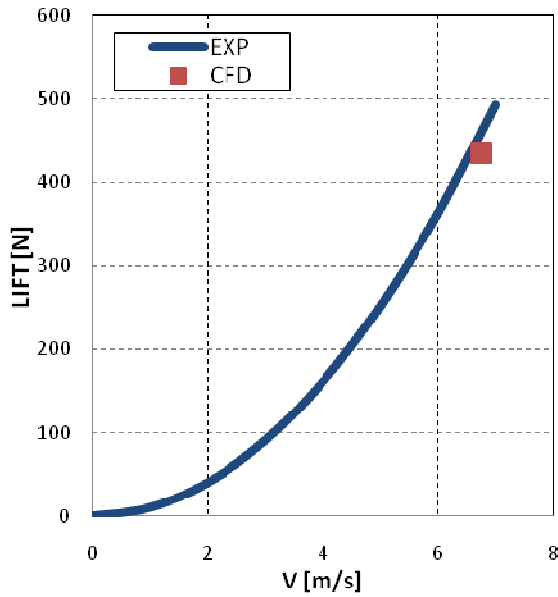


Figure 7: Lift variation with velocity for 3D Twist-11 foil

3.2. (b) Cavitating Flow Results

To simulate a cavitating case on the Twist-11 foil, as on any geometry immersed in the water, the pressure has to be decreased below the vapor pressure so that the fluid will start to cavitate. The analysed conditions in the experiments and computations are as follows: at the inlet an inflow velocity boundary condition of 6.97 m/s, at the outlet a constant pressure boundary of 29.0 kPa and saturation pressure of 2970 Pa. The vapor and water density values are kept the same as in previous cases: 0.023 kg/m³ and 998.0 kg/m³ respectively.

Considering the numerical setting presented previously, the cavitation model is activated and simulations are started up. The calculated cavity volume as well as the frequency of the shedding cycle has been determined. Also, the iso-surface of the vapor pressure is analysed. The numerical results are compared with the experimental data as created by Foeth [7], [8] and [10]. Figure 8 shows the development of the cavity volume in time. This calculation has run initially for some time to obtain the periodic solution of the flow. The cavity shedding period takes 0.032 seconds, which gives a frequency of 31 Hz. The frequency found in the calculations for the shedding matches well with the experimentally determined shedding frequency of the Twist-11 foil of 33 Hz.

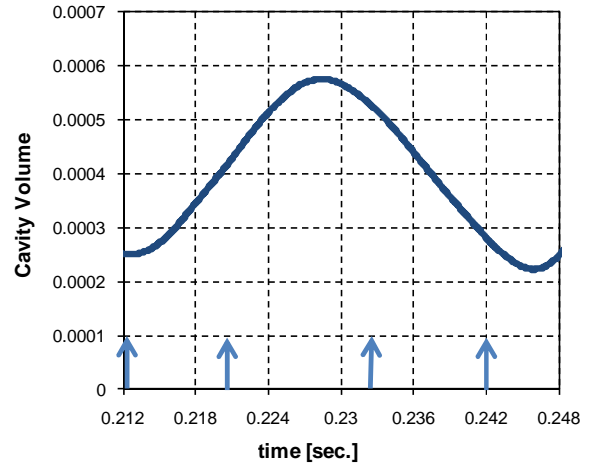


Figure 8: Variation of cavitation volume for 3D Twist-11 foil

The excellent agreement between the calculations and the measurements are confirmed once more in Figure 9 and Figure 10, where the cavity shape is compared for four different times within the shedding cycle.

The numerical results are used to make iso-surface plots of a vapor concentration of 0.01. The experimental results are photographed with high speed cameras. The following times are presented: $t=0.2125s$, $t=0.221s$, $t=0.233s$ and $t=0.242$ seconds. These conditions are marked in Figure 8 with the arrows.

At the first time step, a large leading edge cavity is shown, which is well in agreement with the photo of the experiments. The second picture shows the start of the break-up of the cavity at the mid-span, a large cavity cloud starts to be detached from the main leading edge cavity and the side re-entrained jets are formed. In the third picture at $t=0.233$ seconds the detached cloud travelled downstream and has a shape of a so called “horse shoe” cavity. Also the main leading edge cavity starts to grow back to its maximum length preparing for the next cycle of clouds detachment. In the fourth picture the remaining vapor clouds are travelling downstream, while the leading edge cavity continues to grow and the cycle is repeated from the top.

The agreement between the numerical calculations and the photos from the experiments is very good for all four time steps. Based on these results it is concluded that the RANS CFD method is able to predict the complex 3D cavity shape including the transient shedding behaviour.

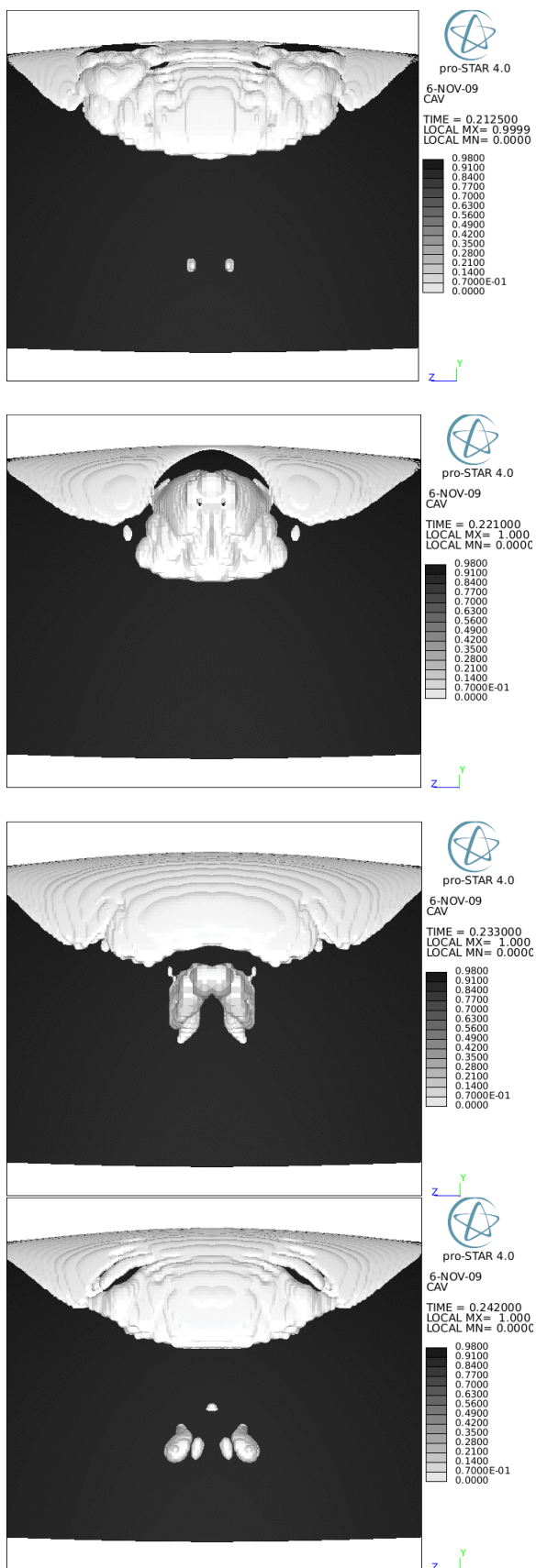


Figure 9: CAV iso-surface=0.01, simulations

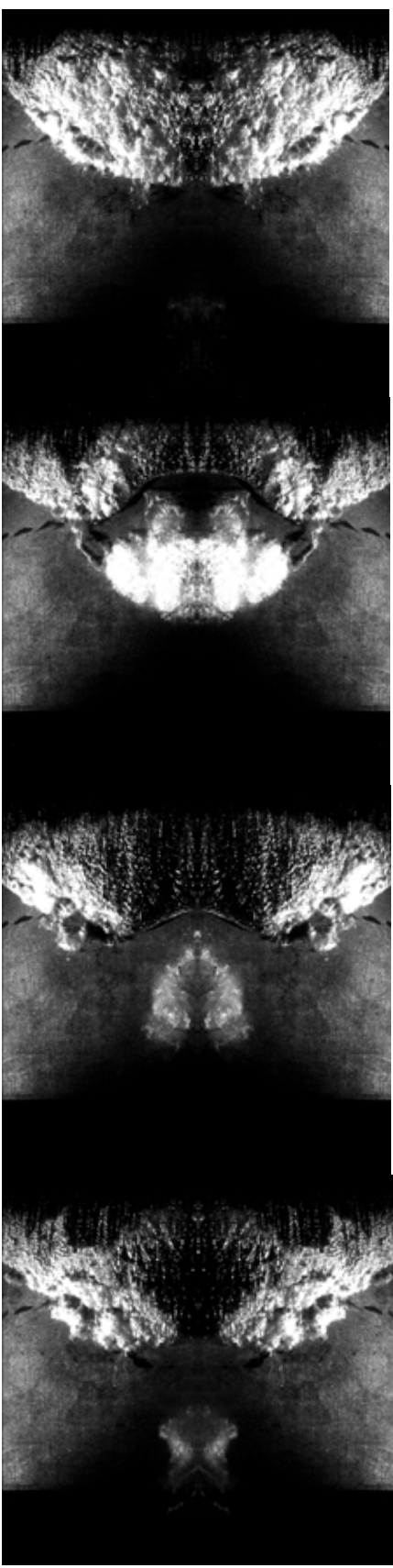


Figure 10: Cavitation visualization, experiments

4. SKEW PROPELLER TEST CASE

The last test case is a real designed propeller study since the goal of the paper is the cavitation modelling on real propeller units.

The investigated propeller geometry is a test case used within the Leading Edge EU project, see [11].

The mesh for the propeller is created with an in-house mesh generator. This program generates a multi-block hexagonal mesh. The mesh near the blades is based on an O-grid type, to maintain control over the quality of the mesh near the blade. Development of the boundary layer along the blade surface is taken into account by wall functions. The requirements for the y^+ values on the blade surface can be met with an acceptable number of cells in the normal direction. Moreover, the aspect ratio and the differences in cell sizes can be kept low.

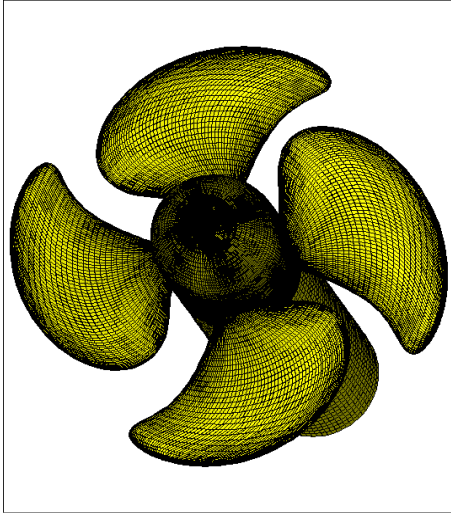


Figure 11: Skew propeller surface mesh

Figure 11 shows the surface mesh of the model scale skew propeller. The four bladed propeller has a diameter of 0.2333m and the RPM used in the model tests and simulations is 840.

4.1 WETTED FLOW RESULTS

The first step in propeller simulations is the comparison of the numerical predicted open water performance with the experimental data. Propeller performances are described by a set of non-dimensional coefficients for advance ratio, thrust and torque as is customary in propeller theory, see Carlton [12]. These coefficients are defined as:

$$J = \frac{v_{ad}}{nD} \quad Kt = \frac{Thrust}{\rho n^2 D^4} \quad Kq = \frac{Torque}{\rho n^2 D^5} \quad (18)$$

where v_{ad} is the advance velocity, n the rotational speed and D the diameter of the propeller. Figure 12 shows the comparison of the calculated and the measured propeller performance. The CFD results are represented with the dashed lines and the experimental data with dots.

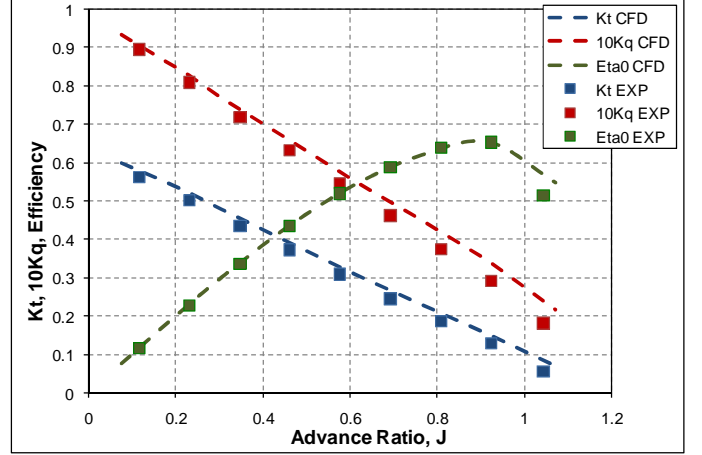


Figure 12: Open water curves, skew propeller model scale

Agreement between the CFD calculations and the experimental data is good for all advance ratios, as from Figure 12. The small differences in the open water curves can be related to the laminar flow present in the model test at propeller low radii.

The main interest of the study is the development of the tip vortex cavitation, therefore one of the blades is refined in the leading edge-tip vortex region. The refinement is done based on the Q-factor parameter and minimum C_p condition, see Banks and Singer [13]. Q-factor is determined via the equation (19) and is used in the present study due to the fact that it has the same level of accuracy in comparison to other tip vortex detection parameters and is also easy to implement.

$$Q = \frac{1}{2} \left[\left(\frac{\partial u_i}{\partial x_i} \right)^2 - \frac{\partial u_i}{\partial x_j} \frac{\partial u_j}{\partial x_i} \right] \quad (19)$$

When $Q > 0$ the rotation is dominant and the region determines a vortex tube. Note that the local vortex refinement is made using cells with high Q-factor values, higher than certain positive values determined by the user. Using this procedure about one million cells are added to the standard mesh within the leading-edge tip vortex region for one blade.

Wetted flow results of the pressure distribution on the skew propeller refined blade at $Kt=0.32$ is shown in Figure 13.

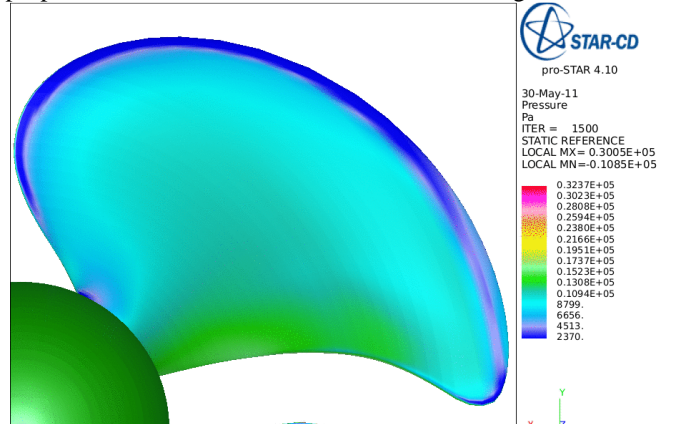


Figure 13: Pressure distribution, wetted flow

At the investigated condition, a low pressure region (below vapour pressure) at leading edge-tip vortex is predicted. This region is expected to cavitate when the cavitation model is enabled.

To determine the tip vortex presence and its downstream development, pressure coefficient and the Q-factor are plotted at three locations behind propeller centre line as shown in Figure 14.

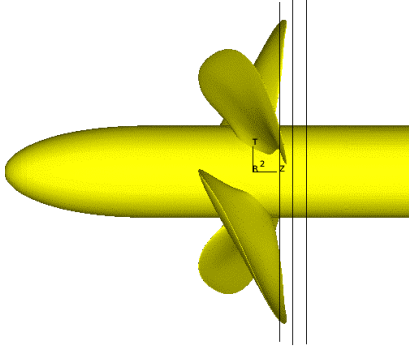


Figure 14: Downstream location planes: $z=20, 30$ and 40 mm

In Figure 15 pressure coefficient and Q-factor through the tip vortex at the three analysed downstream plane locations are shown.

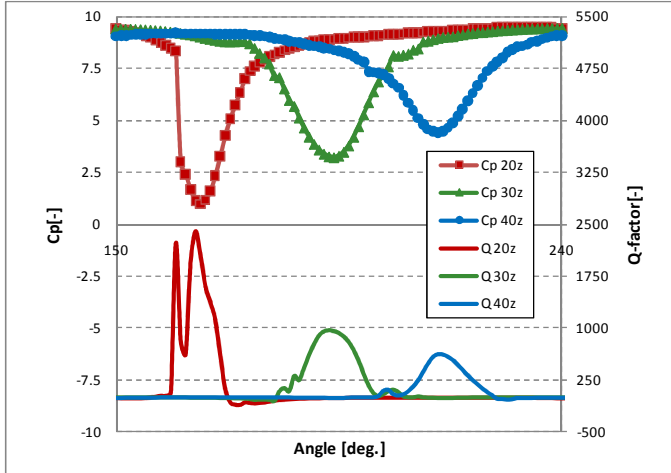


Figure 15: Cp and Q-factor distribution downstream of the skew propeller at $z=20, 30$ and 40 mm

The location of the vortex corresponds to the minimum pressure and the maximum Q-factor parameter values. It is also evident that the tip vortex decays very fast downstream, both on pressure and Q-factor.

4.2 CAVITATING FLOW RESULTS

To investigate the influence of the cavitation on the propeller tip vortex development and its prediction in comparison to the model tests observation, the cavitation model is enabled. The outlet pressure is set to 14500Pa so that the cavitation number is $\sigma=2.27$ for a thrust coefficient $K_t=0.32$, as in the homogenous inflow experiment observations of HSVA [11].

Cavitating results of the propeller pressure distribution contours over the refined blade are shown in Figure 16.

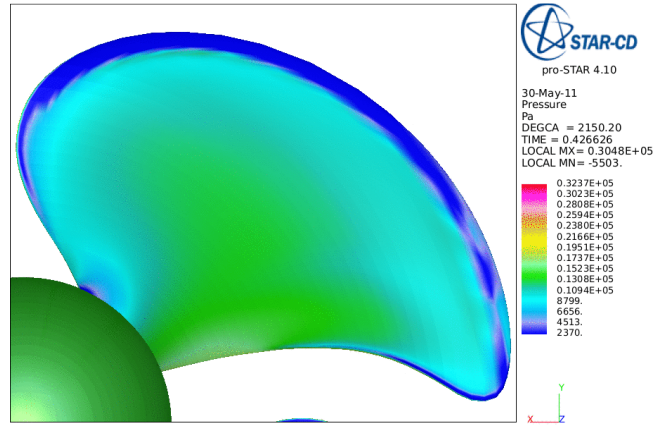


Figure 16: Pressure distribution, cavitating flow

As expected, compared to the wetted flow results (Figure 13), the extend of the minimum pressure region is larger when the cavitation is enabled.

Pressure coefficient downstream of the propeller at same previously presented locations, with and without cavitation is shown in Figure 17.

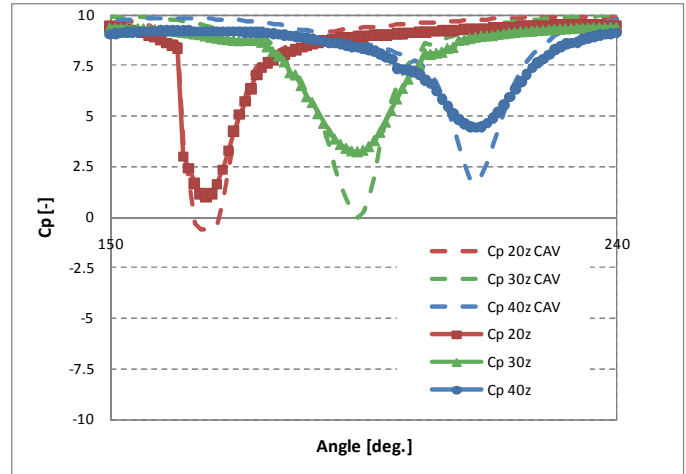


Figure 17: Cp distribution at $z=20, 30$ and 40 mm, wetted versus cavitating simulations

Also, the cavitating minimum pressure is lower than in the wetted flow case.

Moreover, Figure 18 shows the pressure iso-surface equal to the vapour pressure (2370Pa) predicted by computations and Figure 19 shows the cavitation observed in the experiment as from HSVA [11].

Comparing Figure 18 and Figure 19, it is clear that the simulations are able to capture well the location of the leading edge tip vortex cavitation as observed in measurements at the same cavitation number and thrust coefficient. Refining the grid at tip vortex location the extent of the cavity downstream is improved.

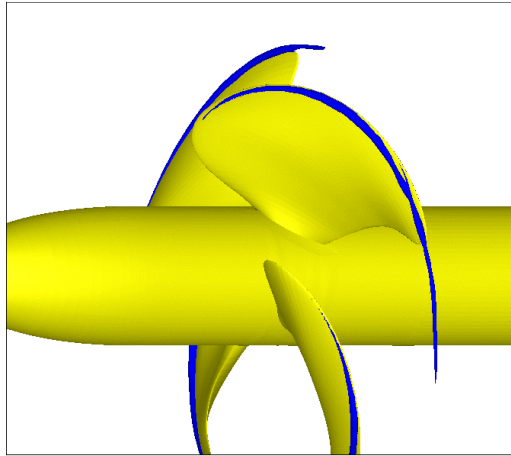


Figure 18: Pressure iso-surface=2370Pa, simulations

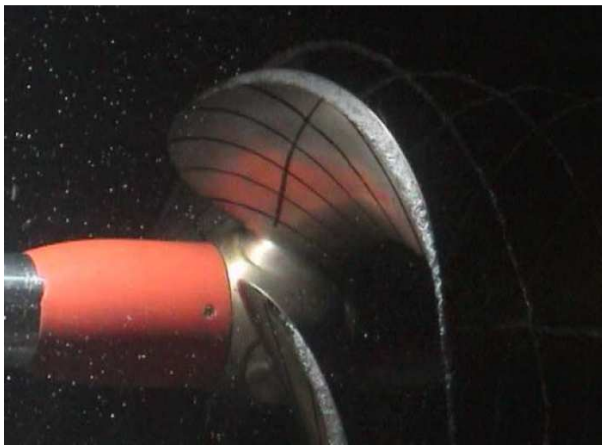


Figure 19: Cavitation visualization, model tests

Note that, the cavitating results over the skew propeller are still under investigation and further post-processing is to be done and published in a later stage, both on model and full scale.

CONCLUSIONS

The goal of the presented research was to develop a reliable method to predict and simulate complex cavitating flows that exist on marine propellers. The CFD method based on RANS mathematical model with a RNG $k-\epsilon$ modified turbulence model and a Rayleigh cavitation model, was assessed on 2D and 3D benchmark geometries with good agreement for cavity shape, forces and shedding frequency.

The validated approach has been applied on a model scale skew propeller test case. Wetted flow simulations compare well with the experiments in term of thrust and torque. While the cavitating simulations are well in agreement with the model tests observations, leading edge-tip vortex cavitation is similar to the experiment results.

The method can be used to predict performances and estimations of the developed cavitation at model scale. In a further validation step the full scale assessment for the skew propeller is still to be done.

REFERENCES

1. STAR-CD, Version 4.02, 'Methodology', CD-adapco Group, 2006
2. Reboud J.L., Stutz B. and Coutier-Delagosha O., 'Two phase flow structure of cavitation: experiment and modeling of unsteady effects', Third International Symposium on Cavitation, 1998
3. Arndt R.E.A., Song C.C.S., Kjeldsen M., He J., and Keller A., 'Instability of Partial Cavitation: A Numerical/Experimental approach', 2000
4. Abbot I. and Doenhoff A., 'Theory of wing sections', 1959
5. Bulten, N. and Oprea A.I., 'Consideration on deviations in torque prediction for propellers and waterjets with RANS codes', RINA, 2005
6. Koop A., 2008, 'Numerical Simulation of Unsteady Three-Dimensional Sheet Cavitation', PhD thesis, at University of Twente, Enschede, The Netherlands, 2008
7. Foeth E. J. 2008, 'The structure of Three-Dimensional Sheet Cavitation', PhD thesis at Delft University of Technology, The Netherlands, 2007
8. Foeth E. J. and van Terwisga T. 2006, 'An attached cavity on a three-dimensional hydrofoil', CAV2006, Wageningen, The Netherlands, 2006
9. VIRTUE (Virtual Towing Tank Utility in Europe) European Commission Project, FP6, <http://www.virtual-basin.org/>
10. Foeth E.J., 'Pressure and Lift Measurements on Twist-11 Hydrofoil', private communication
11. LEADING EDGE EU Project, 'Cavitation inception test of the highly skew propeller', HSVA report, private communication, 2002.
12. Carlton J., 'Marine propellers and propulsion', 2007
13. Banks D.C. and Singer B.A., 1994, Vortex Tubes in Turbulent Flows: Identification, representation, reconstruction Proceedings of IEEE Visualization '94